


2023

Investigations into the electronic and magnetic properties of (CrPS4)_n layers

Alexandria R. Alcantara
University of North Florida

Follow this and additional works at: <https://digitalcommons.unf.edu/etd>

 Part of the [Atomic, Molecular and Optical Physics Commons](#), [Condensed Matter Physics Commons](#),
and the [Quantum Physics Commons](#)

Suggested Citation

Alcantara, Alexandria R., "Investigations into the electronic and magnetic properties of (CrPS4)_n layers"
(2023). *UNF Graduate Theses and Dissertations*. 1173.
<https://digitalcommons.unf.edu/etd/1173>

This Master's Thesis is brought to you for free and open access by the Student Scholarship at UNF Digital Commons. It has been accepted for inclusion in UNF Graduate Theses and Dissertations by an authorized administrator of UNF Digital Commons. For more information, please contact [Digital Projects](#).
© 2023 All Rights Reserved

**Investigations into the electronic and magnetic
properties of $(\text{CrPS}_4)_n$ layers**

Alexandria R. Alcantara

University of North Florida, 2023

**Investigations into the electronic and magnetic
properties of $(\text{CrPS}_4)_n$ layers**

Alexandria R. Alcantara

B.S., University of North Florida, 2021

A Thesis

Submitted in Partial Fulfillment of the
Requirements for the Degree of Master of Science

at the

University of North Florida

2023

Copyright by

Alexandria R. Alcantara

2023

i

APPROVAL PAGE

Master's Degree Thesis

Investigations into the electronic and magnetic properties of $(\text{CrPS}_4)_n$ layers

Presented by

Alexandria R. Alcantara, B.S.

Master's Advisor

Dr. Jason T. Haraldsen

Committee Member

Dr. Michael Lufaso

Committee Member

Dr. Steven Stagon

External Committee Member

Dr. Roxanne Tutchton

External Committee Member

Dr. Christopher Lane

University of North Florida

2023

Dedicated to my loved ones and pets for their moral support.

ACKNOWLEDGEMENTS

A. R. Alcantara acknowledges this work in support of University of North Florida Physics department, D. Santavicca, and Chemistry department, M. Lufaso, along with the Materials Science and Engineering Research Facility for experimental efforts. Theoretical efforts are in support at the Institute of Materials Science at Los Alamos National Laboratory, Theoretical Division-4 staff scientists R. M. Tuthton and C. Lane.

TABLE OF CONTENTS

1. Introduction	2
1.1 Semiconductors	2
1.2 2D Materials	3
1.2.1 2D Semiconductors	3
1.3 2D Magnetic Semiconductors	5
1.4 Chromium Thiophosphate	6
2. Density Functional Theory	9
2.1 What is Density Functional Theory?	9
2.2 Computational Parameters	11
3. Electronic Structure and Band Gap Analysis	13
3.1 Magnetic Ground-State	14
3.2 Electronic Structure	19
3.3 Optical Properties	21
4. Material Synthesis, Characterization, and Experimental Analysis	25
4.1 Sample Preparation	26
4.2 Powder X-Ray Diffraction	26
4.2.1 Synthesis	29
4.3 Structural Characterization	35

5. Electronic Structure of Transition-Metal Doping in CrPS₄	39
5.1 Methodology and Benchmarking	39
5.2 Mn-doped CrPS ₄	40
5.3 Fe-doped CrPS ₄	43
6. Discussion and Conclusion	50
Bibliography	53

LIST OF FIGURES

3.1	Supercell of bulk CrPS ₄ along (a) the <i>c</i> -axis and (b) the <i>b</i> -axis. The Cr atoms are shown in blue, The P atoms in purple, and S atoms in yellow.	14
3.2	(a) Ferromagnetic and the nine antiferromagnetic configurations considered for the ground-state ordering of CrPS ₄ . The green and red arrows represent the positive and negative magnetic moments of Cr in the unit cell, respectively. (b) Ground-state energies relative to the most stable magnetic configuration by calculated by the PBE (green)[1], PBE+U (blue)[2], and SCAN (red) functionals.	15
3.3	(a) The electronic band structure and Brillouin zone route explored (inner panel) for the bulk, bilayer, and trilayer. (b), The total and atomically resolved density of states is related next to the band structure for the bulk. (c) monolayer atomically resolved density of states, with the corresponding (d) monolayer band structure with up (red) and down (green) bands.	20
3.4	Dielectric tensor components of CrPS ₄ FM monolayer showing the real (dashed black line) and imaginary (red) components. The <i>xy</i> and <i>yz</i> components have little to no contribution to the system.	21

3.5	The Kerr parameters of Monolayer CrPS ₄ as a function of energy. The black dashed lines represent the real part, while the red solid line represents the imaginary part. The peaks oscillate as a function of frequency, showing a sensitive dependence toward light.	22
4.1	X-ray diffraction results for the chromium, phosphorus, and sulfur powders next to previous literature results for the pure powders[3, 4, 5]. Of (a) two peaks are shown until the Cr powder begins to spill from the holder from 40 to 75 degree rotation. These two peaks align with the data from the previous literature. The P data in (b) from 0 to 80 degrees rotation shows the wide, rounded peaks caused by the interference of the red powder. The S powder in (c) shows sharp peaks, and matches all peaks from 5 to 60 degrees rotation measured in comparison to the literature. .	27
4.2	The quartz tube before powder insertion. One end of the tube is sealed. Then, approximately 10 cm above the sealed end, the tube is heated for necking to occur.	30
4.3	Bulk CrPS ₄ crystal growth result from furnace 1 (top) and furnace 2 (bottom).	31
4.4	CrPS ₄ crystal shards extracted from the ampoules.	32
4.5	Temperature as a function of distance from the center hot zones of (a) furnace 1, and (b) furnace 2.	32
4.6	Setup for the vacuum sealing process.	33

4.7	Two different tube furnaces are used to produce the CrPS ₄ flakes in the CVT process.	34
4.8	Bulk CrPS ₄ identification using SEM to obtain the atomic ratio from crystal growth for furnace 1 (a) and furnace 2 (b). The stars represent the scan points to obtain the ratios shown in the subsequent intensity plots. . . .	36
4.9	(a) Impurities of Mg and O from sample 1 most likely present in original powder samples due to 1% impurity. (b) Glass shards from the extraction process adhered to the surface of the sample 2 crystal, characterized by Si and O atomic ratios (quartz).	37
5.1	The band structure evolution of CrPS ₄ doped with Mn per each Cr site within the unit cell starting from (a) the mother compound to (h) Cr _{0.13} Mn _{0.88} PS ₄ in steps of $x=0.125$	45
5.2	The density of states for the doped evolution of (a) CrPS ₄ (i) to MnPS ₄ in steps of $x=0.125$	46
5.3	The band structure evolution of CrPS ₄ doped with Fe per each Cr site within the unit cell starting from (a) the mother compound to (h) Cr _{0.13} Fe _{0.88} PS ₄ in steps of $x=0.125$	47
5.4	The density of states for the doped evolution of (a) CrPS ₄ to (i) FePS ₄ in steps of $x=0.125$ showing how the electrons evolve toward the heavier TM compound.	48

5.5 Band gap evolution from CrPS₄ to MnPS₄ (green) and FePS₄ (red) in steps
of $x=0.125$ 49

LIST OF TABLES

3.1	Experimentally determined magnetic properties of bulk CrPS ₄ compared to previous DFT methods highlighting the discrepancy between experimental and current computational magnetic and electronic analyses. The results from the SCAN functional (this study) are also listed.	16
3.2	Energy differences (ΔE) relative to the predicted ground states of eight magnetic configurations for the bulk, bilayer, and trilayer, and two magnetic configurations for the monolayer.	18
5.1	Benchmark results for calculations executed in QuantumATK, vs. previous VASP calculations and experimental values.	40

2D magnetic semiconductors have become of interest due to their magneto-optical effects in lower dimensionality. More specifically, CrPS₄ has gained renewed attention due to its A-type AFM order and air stability prompting analysis and stability studies in its layered forms for use in scalable technology such as spintronic and optoelectronic devices. In this study, we benchmark our approach using the SCAN meta-GGA functional used without U-parameterization on bulk CrPS₄ to demonstrate the accuracy of our methodology to use as tools to go beyond current CrPS₄ theoretical studies. We examine the 2D electronic nature and optical spectrum for use in experimental analysis. We demonstrate the growth and characterization process of bulk CrPS₄ through means of chemical vapor transport and scanning electron microscopy, exhibiting the efficiency of this material for applied cases. We then theoretically model the electronic systems of MnPS₄ and FePS₄ by doping CrPS₄ with Mn and Fe separately to report the changes in state and band gap due to the added valence electrons an effort to add to the transition-metal thiophosphate family as 2D magnetic materials.

Chapter 1

Introduction

1.1 Semiconductors

Insulators with reasonable band gaps have been an essential technology building block since 1947, allowing directionality in electron flow through circuits, formally known as semiconductors[6]. Without a specific energy gap to define a semiconductor from an insulator, the width of the forbidden region between an insulator's lowest unoccupied molecular orbital (LUMO) valence band and highest occupied molecular orbital (HOMO) conduction band provides diversity in the application, and it dictates the unique properties needed for technology. Silicon wafers are widely used as semiconductors in integrated circuits. However, the material fault owes to the inability of size reduction, exhibiting a quantum tunneling effect when linewidths are reduced to 1000 Å (0.25 μm) and below[7, 8]. Related to this limitation, manufacturing of Si wafer fabrication is costly[9, 10].

1.2 2D Materials

The isolation of weak interlayer bonding and high electron mobility of single-layer carbon (graphene) in 2004 prompted interest in condensed matter physics with its cheap and easy material processing and advantageous implementation. The delicate interlayer coupling allows the bulk graphite crystals to be easily exfoliated into atomically thin flakes using the inexpensive mechanical cleavage (scotch-tape) method[11]. Furthermore, the strong hexagonal covalent bonds within the xy plane lead to flexible functionality[12, 13, 14]. Nevertheless, due to its Dirac band structure, graphene cannot be utilized in switching applications. Thus, the production of 2D semiconductors has risen to the forefront of condensed matter study and technological advancement.

1.2.1 2D Semiconductors

Although 2D semiconductors are not found in nature, they can be produced through chemical vapor synthesis and other methods[15, 16, 17]. Specifically, chemical vapor deposition and chemical vapor transport (CVT) are utilized to grow bulk 2D semiconductors, which can then be thinned down from the bulk compound into atomically thin layered structures using the scotch-tape method[18]. With this means of production, 2D semiconductors are predicted to be valid over a wide range of applications such as substrates, nanoelectronics, optoelectronics, and quantum computing[19, 20, 21, 22, 23].

The ease of synthesis and diversity of 2D semiconductors has led to an abundant number of fundamental studies and the design of new devices. Not only does the use of

size-reducing technology from versatile 2D semiconductors improve the efficiency of current technology, these materials are also low-cost, thus providing more abundance in the library of research studies and electronic production, expediting the process of Moore's Law[24].

Recently, these quantum heterostructures with van der Waals interactions have been characterized through modification methods to broaden the understanding of atomically thin materials[25, 26]. Experimental studies have predicted various uses of these materials' advantageous, unique band gaps. In contrast to graphenes' high conductivity caused by the occupation at the Fermi level, causing electrons to move freely, the 2D semiconductor hexagonal boron nitride (HBN) is an electrical insulator with a measured indirect band gap of 5.96 eV, making HBN useful as a substrate or barrier due the valence electrons' substantial energy required to jump to the conduction band[19, 27]; fabrication of two-dimensional van der Waals heterostructures with electronic band gaps between 1-4 eV, such as MoS₂/ZnO thin films harvest visible light by extending the visible light regions between the band gaps, showing perovskite solar cell application[28]. Narrow band gaps, such as few-layer Nb₂SiTe₄ (0.3 eV) exhibit mid-infrared detection, useful in ambipolar transistors[29].

With the success of synthesis and study on 2D semiconductors beginning the framework for sizeable modern devices, attention on 2D materials has expanded into the unique effects within the single and few-layer systems. Transition-metal dichalcogenides (TMDC) are classified as the MX₂ varieties (M = V, Cr, Mn, Fe, Co, Ni,

Cu, Zn) , having a plane of metal ions between chalcogen atoms, causing high electron mobility within the xy plane. The weak interlayer bonding of TMDCs caused by the van der Waals interactions allows diverse synthesis techniques such as exfoliation, epitaxy, and chemical vapor deposition down to unit cell thickness, allowing advantage of the high electron mobility within the few-layer systems[25, 26, 30, 31, 32]. The rich electronic and optical properties of TMDC's in lowered dimensionality have granted the application of 2D semiconductors into solar cells and electrochemical battery improvement[33, 34]. However, TMDC's cannot be implemented into memory devices due to the absence of magnetism.

1.3 2D Magnetic Semiconductors

Caused by the spin of the electrons, magnetic moments are aligned to specific orientations unique to the communication between either long or short-range orders to settle in a ground state of the crystal, giving a total net magnetism of zero. The alignment of these moments can be forced out of their ground state, allowing nonzero net magnetism. This can be achieved through external fields, doping, or similar influence. These moments can be finely tuned within or between each atomic layer of the 2D magnetic material depending on the direction of the applied effect relative to the crystal.

Recently, several reports of new 2D magnetic materials have appeared in literature displaying a rich variety of magnetic structures[17], along with a myriad of competing topological and superconducting phases[35, 36]. The layer-dependent fer-

romagnetism exhibited by these compounds, such as CrI_3 , offers a new pathway for the development of new spintronic devices because of their wide tunability using doping, electric field, light, and pressure [37]. However, the current workhorse CrI_3 , and similar materials, are fundamentally limited due to their extreme sensitivity to air [38], requiring special glovebox environments and capping layers to preserve the material properties. Therefore, it is crucial to identify air-stable 2D ferromagnetic materials to advance the next generation of spintronic, optoelectronic, and future quantum information technologies in general [17].

With the growth of study and discovery of materials exhibiting tunable electronic and magnetic properties, metal-phosphorous compounds, known as thiophosphates, are a newly discovered class within the 2D chalcogenide family. Recent studies propose further potential in energy applications from the thiophosphates suggested through their unique electronic, structural, optical, and magnetic properties[39]. The MPX (X = S, Se, Te) class have been demonstrated through Raman Spectroscopy, indicating a proper photocatalyst light absorption range in the band gap ranging from 1.3 to 3.5 eV [40] showing use in its optical and electronic properties. However, little knowledge has been acquired about the magnetic properties of these ternary compounds.

1.4 Chromium Thiophosphate

CrPS_4 has recently been singled out due to its intrinsic ferromagnetic ordering in the monolayer [41] and robust air-stability [42]. CrPS_4 is not only a strong 2D magnetic

semiconductor candidate for use in enhanced scalable technology but also effective in production. Synthesis techniques yield larger than 60% pure crystal from the initial powder form in the CVT method without the use of a transport agent, making it well-suited for scalable production[43]. These key properties have prompted a number of experimental [43, 44, 45, 46, 47, 48, 49, 50, 51, 52, 53] and theoretical [1, 2, 54, 55, 56] studies. Specifically, CrPS₄ exhibits a canted ferromagnetic order within each van der Waals layer. When stacked, no net magnetic moment is admitted for an even number of layers characteristic of an A-type AFM ground state [57]. The large magnetic polarization on each Cr site ($2.81 \mu_B/\text{Cr}$) produces a 1.40 eV gap in the electronic states, suggesting CrPS₄ is well suited for switching [44] and neuromorphic computing [58] applications.

As of late, the increase in experimental studies on CrPS₄ evidences its usefulness in applications; however, with the motivation to implement this material into technology, theoretical studies have not been prominent. TM-thiophosphates may be highly tunable in optical, electrical, and magnetic properties and thus can be further investigated in theory for the use of other transition metals and their effect on the system. Yet, there exists a significant lack of consideration toward accuracy within the foundational studies from CrPS₄ to prompt these predictions.

The limited theoretical works analyzing CrPS₄ have found mixed success. Density functional theory calculations at the generalized gradient approximation (GGA) level find the experimental A-AFM magnetic ground state. However, the Cr magnetic

moments are underestimated ($2.58 \mu_B/\text{Cr}$), along with the band gap (0.79 eV) by almost a factor of two [1, 57], as expected for Kohn-Sham theory. To remedy this, a Hubbard U parameter has been applied to the Cr-3d states to yield the correct magnetic moment [2]. This correction predicts an X-type AFM ground state in contrast to neutron scattering measurements [57] and an exaggerated band gap of 1.66 eV. Due to the sensitivity of this system, there is currently no theoretical treatment that captures the delicate balance between the charge and magnetic degrees of freedom. Thus, making predictions of magnetoelastic coupling, magnetoresistive switching, and magnetic excitations is challenging.

Chapter 2

Density Functional Theory

2.1 What is Density Functional Theory?

The early 20th century witnessed innovative years contributing to the foundational principles that paved the way for modern-day physics. Quantum mechanics was recognized to explain the nature of electrons with the added effects of the nucleus in a many-body system beyond the Hydrogen model using the Schrödinger equation. Though groundbreaking success came about from the Schrödinger equation, for anything larger than He, hand-written calculations are prohibitively expensive with low efficiency in providing conclusions on the interactions within the chosen system. Thus, approximations for practical methods using quantum mechanics was developed for these complex systems.

The wave function of a N number of electrons within a system is approximated as

$$\Psi(r_1, r_2, \dots, r_N) = \Psi_1(r_1) \dots \Psi_N(r_N), \quad (2.1)$$

where each $\Psi_i(r_i)$ represents one solved electron in the Schrödinger equation having a potential term of the average field felt from the surrounding electrons in the system.

This wave function product is used in the Hartree-Fock method - a method used to determine the approximation of a many-body system in its ground (stationary) state[59]. Hartree assumed that the nucleus and electrons form a spherically symmetric potential field, in which the final field must be 'self-consistent' with the initial field.

The minimum ground state potential energy from the electron-nuclei interaction calculated from the is used as the external potential (the Coulomb potential) for the total energy of a system in which an overall charge density can be defined as the total energy. The total energy can be expressed as a functional (a function of functions), in which the Kohn-Sham density functional theory is now introduced, and expressed as

$$E[\rho] = T_s[\rho] + \int dr v_{ext}(r)\rho(r) + E_H[\rho] + E_{xc}[\rho], \quad (2.2)$$

where T_s is the Kohn-Sham kinetic energy, v_{ext} is the external potential energy, E_H is the Hartree energy, and E_{xc} is the exchange-correlation energy[60]. The exchange and correlation energy for single electrons correct the self-interaction errors from electrons that may occur due to the system being treated as a generalized average.

To further develop approximations for complicated quantum systems, density functional theory (DFT) for electronic systems was introduced by Walter Kohn, Pierre Hohenberg, and Lu Jeu Sham by the 1960s[61]. By treating the system as an overall density $n(r)$ rather than the complicated many-body wave function shown in Eq. 2.1, an approximation within the system can be made to determine the overall electronic structure and energy within the chosen system. The practicality of DFT grew increasing attention as these approximations gave a general sense of the energies for the ground

state of materials as a basis for applications. Over time, these techniques were implemented into computers, where DFT has become an essential tool to solve convoluted systems, including magnetism, relativity, and superconductivity.

2.2 Computational Parameters

CrPS₄ is the first reported metal thiophosphate with a metal-centered octahedral close-packed geometry with sulfur in which its crystal structure was described as having a monoclinic symmetry, with space group *B2/m*. The lattice structure is defined as $a = 10.859\text{\AA}$, $b = 6.128\text{\AA}$, $c = 7.244\text{\AA}$, $\gamma = 91.90^\circ$, and $Z = 4$ [62]. The bulk CrPS₄ obtained from the Inorganic Crystal Structure Database (ICSD), ID number 626520, is used to build the observed atomic positions from neutron scattering measurements[41] and lattice parameters for the bulk benchmarking unit cell and furthermore, to construct the trilayer, bilayer and monolayer structure.

Our calculations were carried out by using the pseudopotential projector-augmented wave (PAW) method [63] implemented in the Vienna *ab initio* simulation package (VASP) [64, 65] with an energy cutoff of 260 eV for the plane-wave basis set. Exchange-correlation effects were treated by using the SCAN meta-GGA scheme [66]. A $6 \times 7 \times 1$ Γ -centered k -point mesh was used to sample the single-, two-, and three-layer structures. A $6 \times 7 \times 5$ mesh was used to sample the slab (bulk) material. The dielectric tensor components were calculated using 1296 virtual states to ensure all bands were accounted for. Spin-orbit coupling effects were included self-consistently, which are

calculated within the Wigner Seitz radius to capture the local magnetic moment without contamination from the surrounding environment. The magnetism is driven by the Cr^{3+} valence electrons, with three $3d$ electrons spread in the t_{2g} sub-orbital occupations as defined by the Pauli-Exclusion Principle that yields a spin moment of $S = 3/2$. A vacuum spacing of 19 \AA was used to ensure no interactions occurred between the periodic images for the single-, two-, and three-layer unit cell model. A total energy tolerance of 10^{-6} eV was used as convergence to determine the self-consistent charge density. For these parameters, we will investigate the electronic and magnetic ground state of the 2D magnetic semiconductor, CrPS_4 , with various sections adapted from the manuscript , '*Parameter free treatment of a layered correlated van der Waals magnet : CrPS_4* ' (Alcantara *et. al*) [67].

Chapter 3

Electronic Structure and Band Gap Analysis

-Figure 3.1 shows the crystal structure of bulk CrPS₄ along the (a) *c*- and (b) *b*-axes. The chromium atoms (blue) sit on an orthorhombic lattice and are octahedrally coordinated by sulfur atoms (yellow) that are slightly distorted off-center. Due to the orthorhombic Bravais lattice, the Cr atoms form linear chains of strong inter-site coupling along the *b*-axis, with weaker inter-chain interactions along the *a*-axis. The phosphorus atoms (purple) sit at the center of a sulfur tetrahedral cage, where its position alternates between above and below the Cr layer following the distorted sulfur octahedra. This puckering of the phosphorus sites constrains the primitive monoclinic unit cell to accommodate four Cr atoms, rather than simply one. Moreover, the phosphorus atoms form a bridge between Cr chains, thereby facilitating weak inter-chain interactions. Along the *c*-axis, the atomically-thin layers are found to stack in an AA manner with a clear 3.75 Å vdW gap separating neighboring layers. This suggests the electronic states should be predominantly 2D in nature with very weak k_z dispersion.

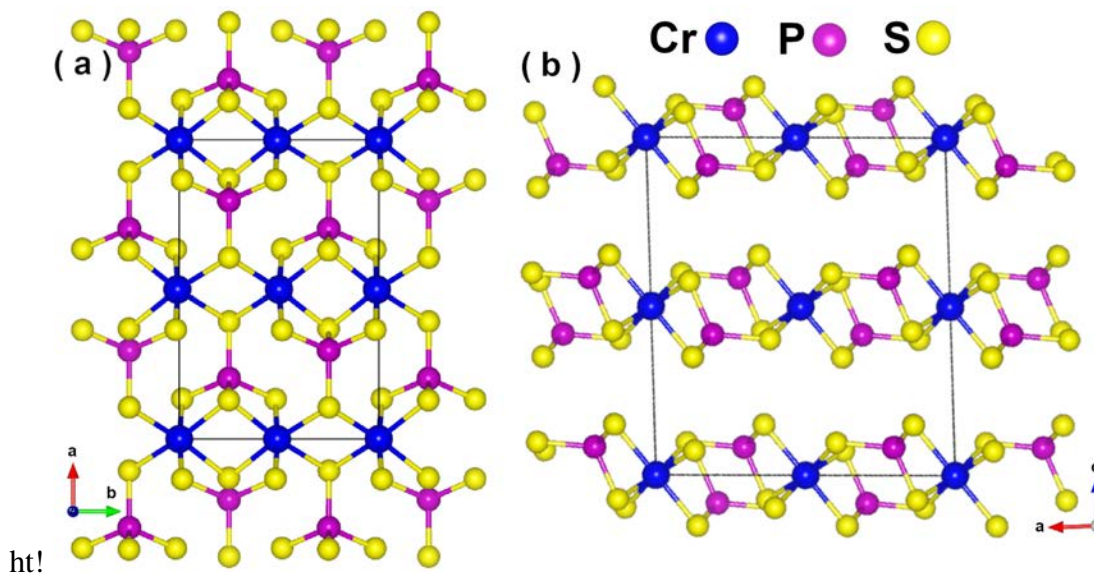


Fig. 3.1: Supercell of bulk CrPS₄ along (a) the *c*-axis and (b) the *b*-axis. The Cr atoms are shown in blue, The P atoms in purple, and S atoms in yellow.

3.1 Magnetic Ground-State

We begin this study with calculating the magnetic ground state of the system by using the computational parameters discussed in Ch. 2.2. By first calculating the experimentally observed ground state for the bulk CrPS₄ compound, we set an appropriate foundation for the theoretically determined few-layer system.

-Figure 3.2 (a)-(b) shows the various collinear commensurate magnetic orders studied in bulk CrPS₄, along with the corresponding relative total energies of each magnetic configuration with the values from previous PBE and PBE+U studies overlaid. Since the bulk primitive cell of CrPS₄ has eight Cr atoms spanning two layers, nine distinct commensurate magnetic orders may be accommodated. To enumerate the

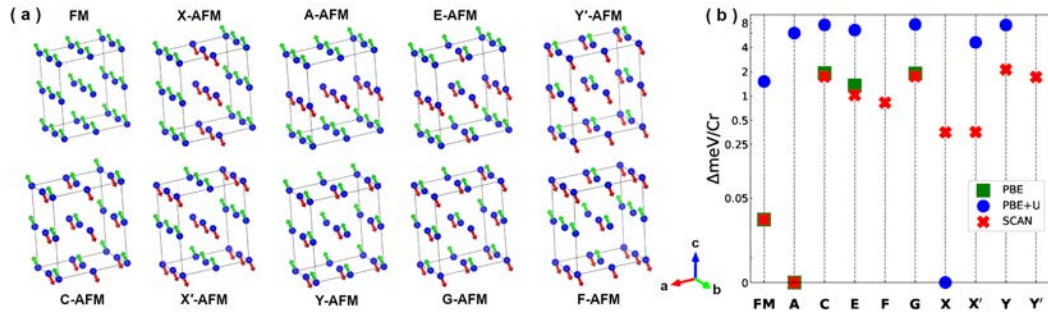


Fig. 3.2: (a) Ferromagnetic and the nine antiferromagnetic configurations considered for the ground-state ordering of CrPS₄. The green and red arrows represent the positive and negative magnetic moments of Cr in the unit cell, respectively. (b) Ground-state energies relative to the most stable magnetic configuration by calculated by the PBE (green)[1], PBE+U (blue)[2], and SCAN (red) functionals.

phases, we initially assume FM coupling between all Cr sites to produce an FM phase with all magnetic moments pointing slightly canted off the c -axis. If inter-chain (intra-chain) interactions are switched to AFM, then we perturb away from the FM phase yielding a stripe-like X-type (Y-, Y'-type) AFM order that varies along the a -axis (b -axis). Additionally, swapping the FM inter-layer coupling for AFM triggers an A-type AFM state where the direction of the magnetic moments alternates with CrPS₄ layers. Finally, by combining inter- and intra-chain, and inter-layer couplings, the E-, F-, C-, X'-, and G-type AFM states are found. Furthermore, this weak interlayer coupling is also reflected in the interlayer binding energy,

Table 3.1: Experimentally determined magnetic properties of bulk CrPS₄ compared to previous DFT methods highlighting the discrepancy between experimental and current computational magnetic and electronic analyses. The results from the SCAN functional (this study) are also listed.

Bulk CrPS ₄	SCAN (this study)	Experiment [41]	PBE [1]	PBE+U [2]
Ground state	A-AFM	A-AFM	A-AFM	X-AFM
Band gap (eV)	1.34	1.40	0.79	1.66
Moment (μ_B/Cr)	2.78	2.81	2.58	3.00

$$E_{bind} = \frac{E_N - NE_1}{Nn}, \quad (3.1)$$

where N is the number of layers, E_N is the total energy for an N -layer slab of CrPS₄, and n is the number of atoms in a single layer.

Figure 3.2 (b) plots the energy of each magnetic configuration relative to the ground state using PBE [1] (green squares), PBE+ U [2] (blue circles), and SCAN (red \times) functionals. PBE correctly captures the correct ground state magnetic order and predicts the FM phase is only 2.00 meV higher in energy. Moreover, the magnetic moment direction and magnitude, though slightly underestimated [Table 3.1], are also in good accord with experimental values. The remaining magnetic arrangements considered (C-, E-, and G-AFM) are separated from the A-AFM phase by ~ 2 eV/Cr, making them

irrelevant to the low energy degrees of freedom. The close energetic proximity of FM and A-AFM states suggests a delicate balance between AFM and FM coupling between the CrPS₄ layers. Despite PBE's success in describing the magnetic state, it severely underestimates the electronic band gap [Table 3.1] as is expected since the Kohn-Sham eigenvalues do not provide the value of the gap. To improve upon the PBE description of the ground state, a Hubbard U was included on the Cr- d by Joe *et al.* [2]. By applying a U , charge localization is enhanced on the Cr atomic sites, increasing the magnetic moment and band gap [Table 3.1]. Interestingly, the added Hubbard parameter disrupts the inter- and intra-layer exchange couplings ratio, thus predicting an X-AFM ground state with all other phases at least 1.5 eV/Cr higher in energy.

We find the SCAN density functional to remedy the pitfalls of both previous approaches without introducing any empirical parameters. Specifically, SCAN recovers the experimental A-AFM ground state ordering and predicts magnetic moments of 2.81 μ_B tilted off the c -axis by 71.6° in excellent accord to the experimental values [41]. Moreover, the A-AFM state stabilizes with a band gap of approximately 1.34 eV that opens up around the Fermi energy of the NM system. This gap is in good agreement with optical data [57]. We note that since SCAN is constructed within the generalized Kohn-Sham (gKS) scheme[68], the band gap has restored meaning and is now equal to the fundamental band gap in the solid [69]. Therefore, the holistic agreement between magnetic and electronic properties in CrPS₄ stems from the reduction in self-interaction error in SCAN compared to PBE and is not accidental.

Table 3.2: Energy differences (ΔE) relative to the predicted ground states of eight magnetic configurations for the bulk, bilayer, and trilayer, and two magnetic configurations for the monolayer.

Magnetic order	Bulk ΔE (meV/Cr)	Trilayer ΔE (meV/Cr)	Bilayer ΔE (meV/Cr)	Monolayer ΔE (meV/Cr)
FM	2.00	7.20	5.70	0.00
A-AFM	0.00	0.00	0.00	-
C-AFM	139	213	143	86.6
E-AFM	82.5	126	82.3	-
G-AFM	141	212	145	-
X-AFM	28.3	258	173	-
X'-AFM	28.5	258	175	-
Y-AFM	171	44.9	31.6	-

Table 3.2 presents the relative total energy of each magnetic configuration with respect to the A-AFM state for various sample thicknesses. The A-AFM phase is found to be the ground state for all layered films studied, with a robust FM order stabilizing in the monolayer. By comparing the energy of each magnetic state, the FM phase is the closest competing magnetic state, with only $\approx 2-7$ meV/Cr energy separation irrespective of thickness. Curiously, the energy difference between A-AFM and FM arrangements follows a non-monotonic evolution with several CrPS₄ layers. Similarly, the remaining magnetic orders farther away from the ground state display a dependence on the number of layers that is quite sensitive. In particular, the X- and Y-AFM phases interchange energetic ordering from the bilayer to the bulk systems. This suggests the screening environment may play a key role in tuning the relative strength between the inter- and intra-chain interactions. Additionally, by comparing C-, G-, X-, and X-AFM configurations, the interlayer exchange couple is seen to be on the order of a few meV/Cr.

3.2 Electronic Structure

-Figure 3.3 shows the (a) electronic band structure and (b) atomically resolved density of states of CrPS₄ in the A-AFM phase for the bulk, bilayer, and trilayer, with separately the (c) monolayer atomically resolved density of states, and corresponding (d) monolayer band structure. For the multi-layer structures, the A-AFM magnetic order stabilizes a direct 1.34 eV band gap at Γ in the Brillouin zone of bulk CrPS₄. Interest-

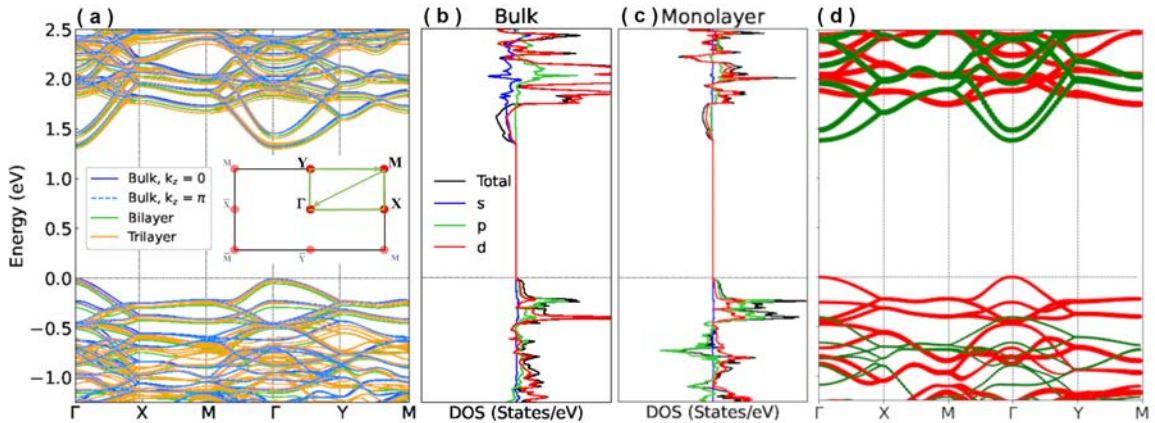


Fig. 3.3: (a) The electronic band structure and Brillouin zone route explored (inner panel) for the bulk, bilayer, and trilayer. (b), The total and atomically resolved density of states is related next to the band structure for the bulk. (c) monolayer atomically resolved density of states, with the corresponding (d) monolayer band structure with up (red) and down (green) bands.

ingly, the band dispersions appear to be insensitive to k_z dispersion, in line with very weakly interlayer coupling. Specifically, the bands for $k_z = 0$ (solid blue lines) and $k_z = \pi$ (dashed blue lines) are essentially identical, where minor deviations are only exhibited along the M- Γ -Y path in momentum space. As CrPS₄ is thinned, the band structure for the trilayer (orange solid lines) and bilayer (green solid lines) appears to be stationary and display nearly identical eigenvalues throughout the Brillouin zone, except for a slight rigid shift (~ 70 meV) due to the non-monotonic evolution of the gap. In contrast, the monolayer [Fig. 3.3(d)] displays an indirect band gap of 1.745 eV characterized by momentum-shift of (π, π) . The corresponding atomically resolved

density of states [Figure 3.3(b) and (c)] reveals the valence bands to be predominantly composed of sulfur character 99%, whereas the conduction band is dominated by Cr states 27%. This stacking-of-states follows the Zaanen-Sawatzky-Allen classification of a charge-transfer insulator [70]. Therefore, in contrast to the Mott-Hubbard insulator, when a hole is doped into CrPS₄, the carrier would sit on the sulfur atomic sites rather than in the Cr sites. The percentage of metal cation (ligand anion) weight in the conduction (valence) band is relatively constant across the bulk, single-, and few-layer systems.

3.3 Optical Properties

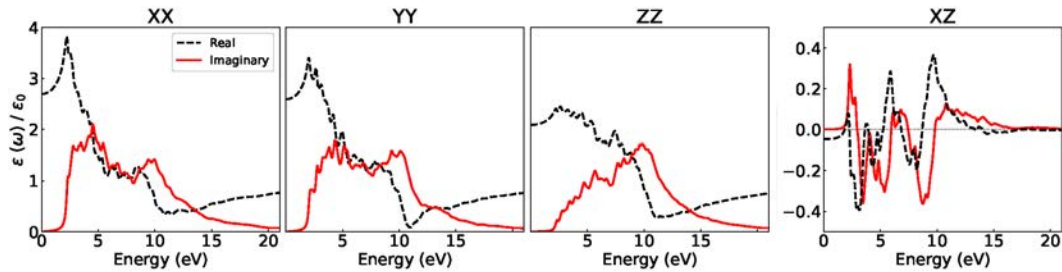


Fig. 3.4: Dielectric tensor components of CrPS₄ FM monolayer showing the real (dashed black line) and imaginary (red) components. The xy and yz components have little to no contribution to the system.

To accelerate the design of the next generation of microelectronic devices, it is necessary to be able to cross-validate both theoretical calculations and experimental measurements. To this end, we first must judge the quality of our theoretically obtained

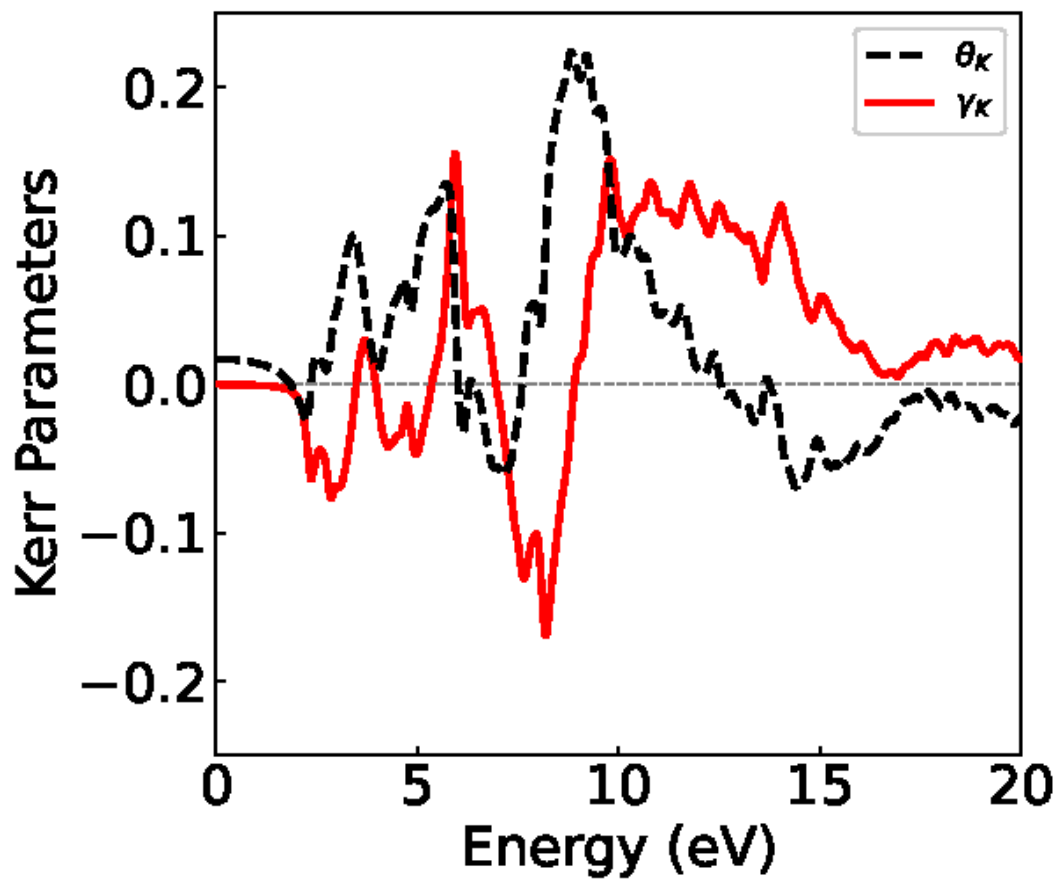


Fig. 3.5: The Kerr parameters of Monolayer CrPS₄ as a function of energy. The black dashed lines represent the real part, while the red solid line represents the imaginary part. The peaks oscillate as a function of frequency, showing a sensitive dependence toward light.

description of CrPS₄. To address this issue we calculate the dielectric tensor – a key ingredient in the interaction between light and matter – and compare the results to experimental observations.

Figure 3.4 presents the non-zero matrix elements of the dielectric tensor (real and imaginary components) as a function of energy for a single layer of CrPS₄. Two main blocks of transitions are seen spanning ≈ 2 eV - 6 eV and ≈ 9 eV - 11 eV in the imaginary part of the xx and yy tensor components. In contrast, $\varepsilon_{zz}^{(2)}$ displays a very weak leading edge of transitions due to the 2D nature of the material and only retains the broad peak centered at 10 eV. Additionally, the sharp leading edge at ≈ 2 eV in $\varepsilon^{(2)}$ generates a strong polarization peak in $\varepsilon^{(1)}$ through the Kramer-Kronig relation. On average, the indicated peak structure is in good accord with optical spectroscopy reports [45].

Compared to Fig. 3.3, the sharp transition edge at ≈ 2 eV is produced by promoting an electron from the valence- to conduction-band edges along X-M (Y-M). The higher energetic transitions originate from bands 5.0 eV below the Fermi level connecting to the flat conduction bands along X-M and Y-M. Furthermore, our theoretically predicted electronic band gap is in very good agreement with the leading edge of the optical conductivity [57].

As a consequence of the canted ferromagnetic, the off-diagonal xz component of the dielectric tensor exhibits a non-negligible response. Such a response may induce an appreciable Kerr angle in the polarization of the light reflected from a magnetic

CrPS₄ layer. This makes the optical Kerr effect particularly useful in giving direct insight into the local, microscopic magnetism [71] and time-reversal symmetry-breaking condensed-matter systems in general [72].

To estimate the Kerr response of CrPS₄, we compute the complex Kerr parameters according to the equation

$$\psi_k = \theta_K + i\gamma_K = \frac{-\varepsilon_{xz}}{(\varepsilon_{xx} - 1) \sqrt{\varepsilon_{xx}}}, \quad (3.2)$$

which is the standard expression for the polar geometry in the small angle limit [73]. Here, the photon propagates along the y direction and describes a linearly polarized wave with the electric field along the x direction.

Figure 3.5 shows the real and imaginary Kerr parameters θ_K and γ_K , respectively, as a function of frequency. Both Kerr parameters oscillate about zero displaying a quite sensitive dependence on the frequency of light. Specifically, θ_k and γ_k change sign at ≈ 2 eV, followed by a number of additional fluctuations about zero until a maximum in both signals is achieved near 9 eV. Above 9 eV, the Kerr parameters vary more smoothly with frequency. Additionally, θ_K and γ_K appear to be completely out of phase for all frequencies studied. Such a line shape in the Kerr signal is quite different from bulk 3d magnetic, e.g. Fe, Co, and Ni, and more akin to other 2D magnets, e.g. NiPS₃ [74].

Chapter 4

Material Synthesis, Characterization, and Experimental Analysis

In this chapter, we demonstrate CrPS₄ to be real material beyond theory by processing and characterization of the bulk crystal. By utilizing the chemical vapor transport method and scanning electron microscopy, we exhibit the cheap, efficient, and effectiveness of growing CrPS₄ for use in applications.

We began the materials processing of the bulk CrPS₄ crystal starting with separate powder samples of chromium, red phosphorus, and sulfur. We ensure the powders used are the expected elements by means of X-ray diffraction (XRD) and compare our results to previous literature. After confirming the elements, we fashion the powders into a 1:1:4 ratio and sealed the powders into two quartz ampoules in preparation for the CVT method. We use two furnaces to compare the effects of temperature gradients along the furnaces for crystal growth. Synthesis was allowed to take place for five days, during which the ampoules were removed and allowed to cool for two days.

Scanning electron microscopy was used to characterize the resultant crystal formation. Our results showed the topological data received from this material is signified to be the bulk formation of CrPS₄.

4.1 Sample Preparation

Powders are provided by BeanTown Chemical Corporation. The powders are then inspected by means of powder XRD using the Shimadzu XRD 6100 to ensure the correct raw elements are used. The raw elements are then weighed in a 1:1:4 ratio for Cr (99% purity), red P (99% purity), and S (99.5% purity), respectively, relative to their atomic masses. The glass quartz tubes are provided by McMaster-Carr. Two quartz tubes were used and were annealed and sealed first at one end. 11 cm and 12 cm above the sealed end; the tubes intentionally experienced necking through heat application. The powders are introduced into the cavity through a straw to avoid particles attaching to the sides of the ampoule. The ampoules are then vacuum sealed to 20 mTorr with an Ar gas supply to flush the systems. After four cycles of the Ar gas supply, the necking region of the ampoules are again annealed and vacuum-sealed. The ampoules are put into separate tube furnaces, which will further be mentioned as furnace 1 (ampoule 1) and furnace 2 (ampoule 2). Furnace 1 is homemade and furnace 2, is provided by the University of North Florida Chemistry Department. The elements were left to bake at 700 degrees C for five days and then left to cool for two days. The bulk crystals were extracted and inspected using energy dispersive spectroscopy in the Tescan MIRA3 FE-SEM.

4.2 Powder X-Ray Diffraction

X-rays shined on a crystal result in unique diffraction patterns that are characteristic of the structure. Specifically for powder XRD, diffraction is obtained from a powder sam-

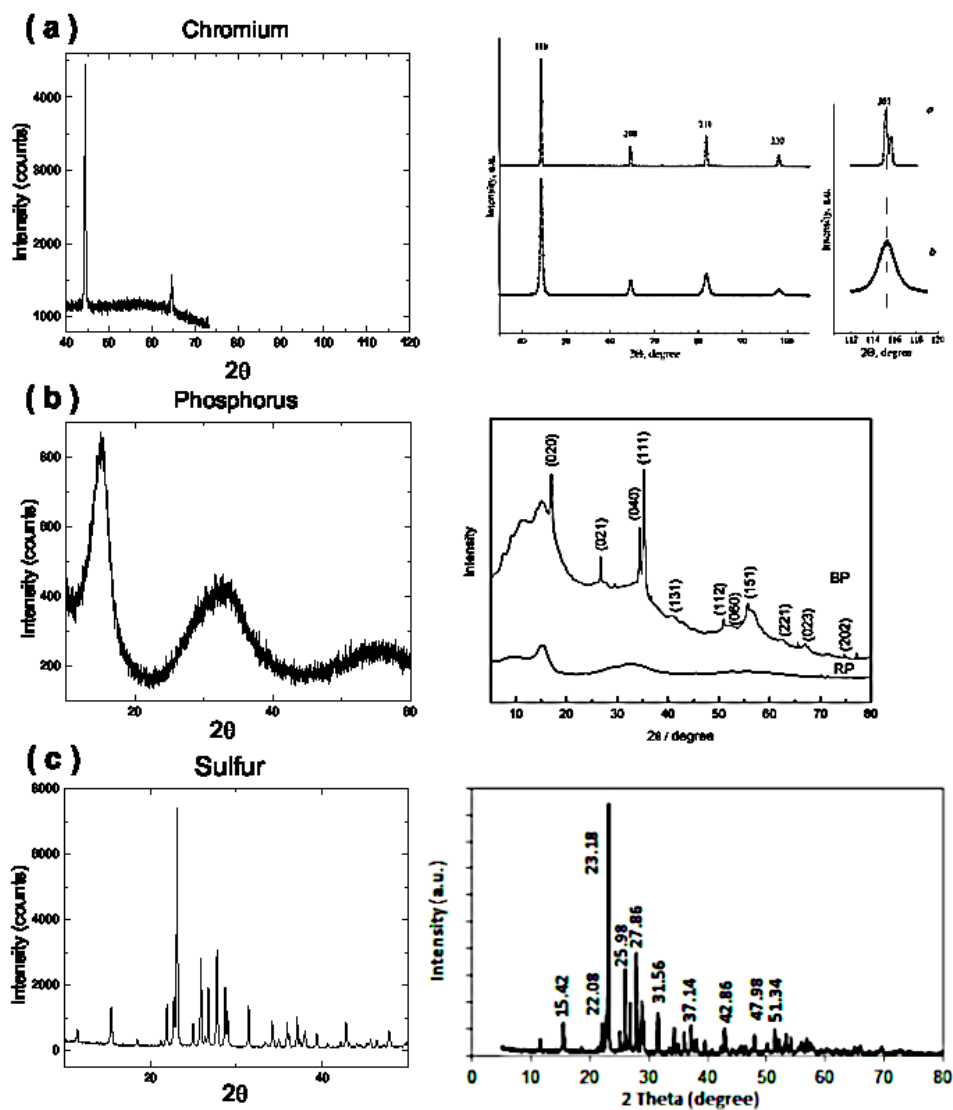


Fig. 4.1: X-ray diffraction results for the chromium, phosphorus, and sulfur powders next to previous literature results for the pure powders[3, 4, 5]. Of (a) two peaks are shown until the Cr powder begins to spill from the holder from 40 to 75 degree rotation. These two peaks align with the data from the previous literature. The P data in (b) from 0 to 80 degrees rotation shows the wide, rounded peaks caused by the interference of the red powder. The S powder in (c) shows sharp peaks, and matches all peaks from 5 to 60 degrees rotation measured in comparison to the literature.

ple rather than a single crystal. This method is often more convenient since it does not require a single, individual crystal. The compounds are identified by using a database of unique diffraction patterns. Along with this, impurities can also be identified from the pattern. Diffraction is determined using Bragg's Law. Bragg's Law is defined as

$$2d\sin\theta = n\lambda, \quad (4.1)$$

where d is the distance between crystal planes, θ is the x-ray incidence angle, n is an integer, and λ is the sample wavelength. Diffraction occurs when the atomic spacing is close to the radiation wavelength. Constructive interference is shown as a peak, and destructive interference appears as no peak.

Within the diffractometer, an x-ray source (Cu_α) is angled at the sample stage, holding the element powder. The stage is chosen to be rotated between angles specific to the samples' previous literature. The detector reads the intensity of the x-ray received at 2θ from the source path.

The diffraction results from the Cr, S, and P powders are shown in Fig. 4.1. The intensities are compared to previous literature on the right. Fig. 4.1 (a) shows the results for the Cr powder. Only two peaks are recorded from the run due to the powder spilling from the sample holder at an angle of 65 degrees, as seen from the linear decrease in intensity. The first two peaks are shown to be similar to previous data, with a large peak at 45 degrees and a smaller peak at the second recorded peak at 65 degrees. These angles represent the crystal plane existing at 45 degrees for the

$\langle 110 \rangle$ plane and the $\langle 200 \rangle$ plane at the 65-degree peak. Although the characterization process recorded only two peaks, they can be presumed to be Cr peaks. Fig. 4.1 (b) shows the diffraction results for the red P powder. When compared to previous data, peaks occur at approximately 18 degrees, 36 degrees, and 56 degrees. In reference to the XRD results in previous literature, note the bottom diffraction pattern is the red phosphorus. This XRD pattern shows the amorphous, polymer-like structure, known to be polymer-like with P_4 tetrahedral bonds. Fig. 4.1 (c) shows the results for the sulfur powder.

4.2.1 Synthesis

Chemical vapor deposition is usually the conventional method to grow crystals; however, ternary compounds such as $CrPS_4$ cannot be grown this way, thus, CVT is instead used for the synthesis of three-element compounds. To synthesize these crystals, a quartz ampoule must be used owing to a higher heat capacity (741 J/gK), withstanding temperatures up to 1100 degrees C in comparison to the commonly used borosilicate glass (0.83 J/gK)[75, 76].

In order to vacuum seal the tubes for the synthesis process, the tubes are annealed and heated at one end and tapered 11 cm and 12 cm above the sealed end as seen in Fig. 4.2. The necking process to taper the cross-sectional area is to ensure less challenge during the sealing of this area when under vacuum.

The Cr, S, and P powders are weighed at a 1:1:4 ratio, respectively, according to



Fig. 4.2: The quartz tube before powder insertion. One end of the tube is sealed. Then, approximately 10 cm above the sealed end, the tube is heated for necking to occur.

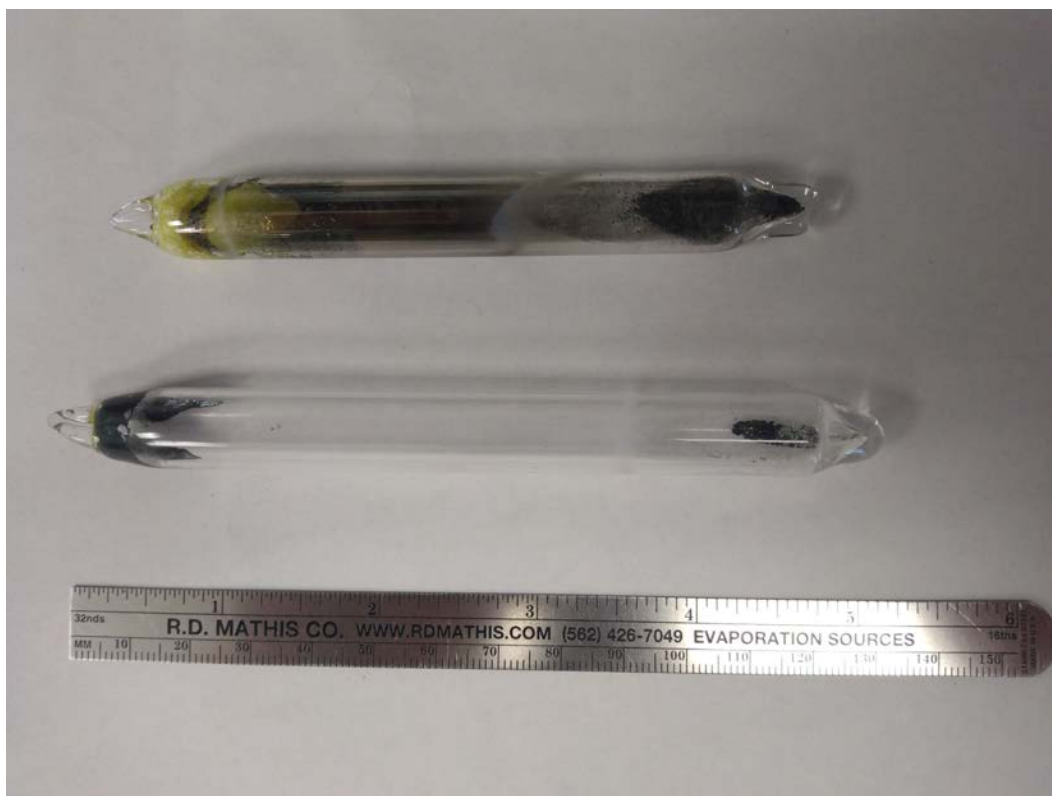


Fig. 4.3: Bulk CrPS₄ crystal growth result from furnace 1 (top) and furnace 2 (bottom).



Fig. 4.4: CrPS₄ crystal shards extracted from the ampoules.

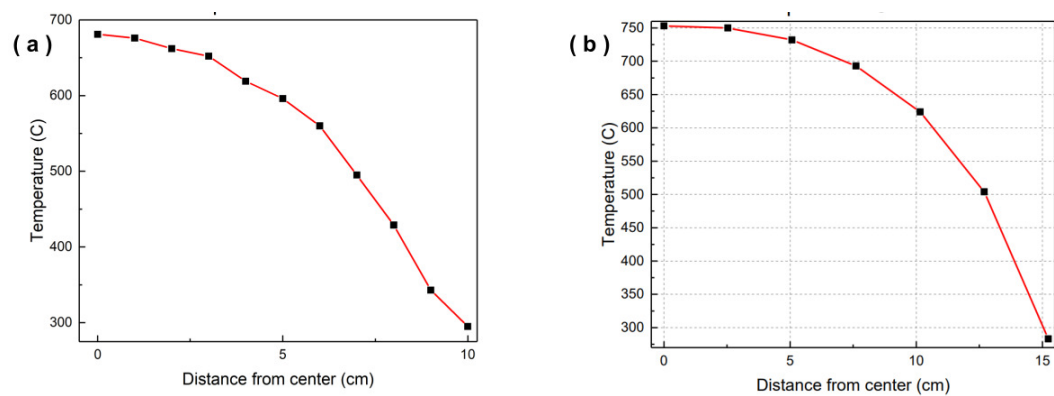


Fig. 4.5: Temperature as a function of distance from the center hot zones of (a) furnace 1, and (b) furnace 2.



Fig. 4.6: Setup for the vacuum sealing process.

their atomic mass. The powders were inserted into two separate prepared quartz tubes using a straw to reduce any particles attaching to the sides of the glass. After insertion, the glass tubes are attached to the Agilent Technologies vacuum pump and flushed with Ar gas for four cycles until a vacuum of 20 mTorr is reached. The setup can be seen in Fig. 4.6.

Before both ampoules are put through the CVT process, the temperature gradient of the two tube furnaces is plotted to ensure the transport along the ampoules is efficient to carry the elements once in a gaseous state. Fig. 4.5 (a) shows the temperature gradient for tube furnace 1, and Fig. 4.5 (b), tube furnace 2. Referencing previous

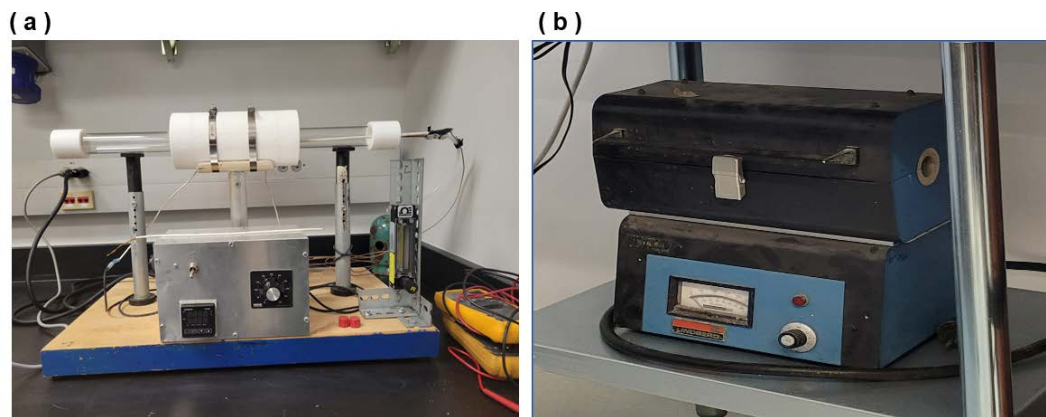


Fig. 4.7: Two different tube furnaces are used to produce the CrPS_4 flakes in the CVT process.

literature[42, 58], the temperature gradient should maintain a decrease of only 100 degrees C between the length of the ampoules (4.5 and 5.5 cm). As seen in Fig. 4.5 (a), the temperature drops from 680 degrees C to 580 degrees C, measured from the hot zone (center of the tube furnace) to 5.2 cm from the hot zone. The temperature gradient from furnace 2 hot zone drops from 750 degrees C to 650 degrees C at 8.5 cm. Due to the difference in temperature gradients, the shorter ampoule (11 cm) is chosen to be placed in tube furnace 1, and the longer ampoule (12 cm) is chosen for tube furnace 2. Both furnaces can be seen in Fig. 4.7.

A quartz ampoule in which the raw elements in powder form are inserted at one end. The ampoule is vacuum-sealed and placed in a furnace between a temperature zone of 700 to 750 $^{\circ}\text{C}$ to form the crystal. The synthesis completes a few mm of crystal compound at the opposing end of the ampoule after approximately one week. The phosphorus and sulfur are transitioned into a gaseous state at the high-temperature

zone and begin to interact with the chromium. Chromium is known to begin transitioning into a paramagnetic phase at the Neel temperature of 38.5 C, thus the transition metal is more likely to ionize and share valence electrons with the P and S gas at this temperatures[77]. The exothermic process is quick to happen for CrPS₄. The vapors appear almost immediately.

After five days, the furnaces were shut off, and the ampoules were allowed to cool for two days. The resulting yield is shown in Fig. 4.3. Ampoule 1 (top) in Fig. 4.3 shows sulfur build at the end placed in the hot zone of furnace 1. In comparison to ampoule 2 (bottom), the yield is significantly less due to a less stable temperature. The cooler end of both ampoules show extra phosphorus transfer. The crystals grew nearer the hot end (around 2 cm from the hot end) where the powders were originally placed.

4.3 Structural Characterization

To ensure the proper atomic lattice is formed, SEM is used to identify the periodic ratio of a bulk sample after removal from the quartz ampoules. SEM identifies the chemical composition of a selected area. The images produced are by electrons backscattering on the sample, requiring a stable room environment in which this sample is held under a vacuum. It then scans across the sample row-by-row, and the different signals collected from the image. These signals are caused by the sample interacting with the electron beam. The information that is recorded is the morphology (size, shape, and arrangement), crystallographic information (arrangement of atoms and degrees of order),

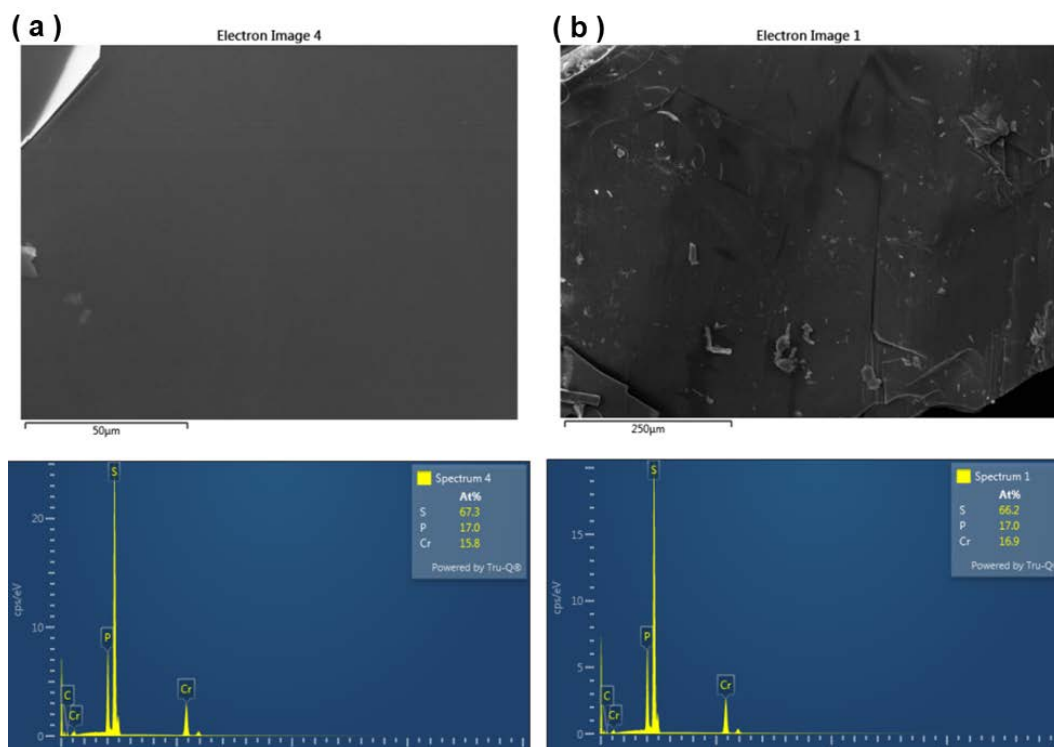


Fig. 4.8: Bulk CrPS₄ identification using SEM to obtain the atomic ratio from crystal growth for furnace 1 (a) and furnace 2 (b). The stars represent the scan points to obtain the ratios shown in the subsequent intensity plots.

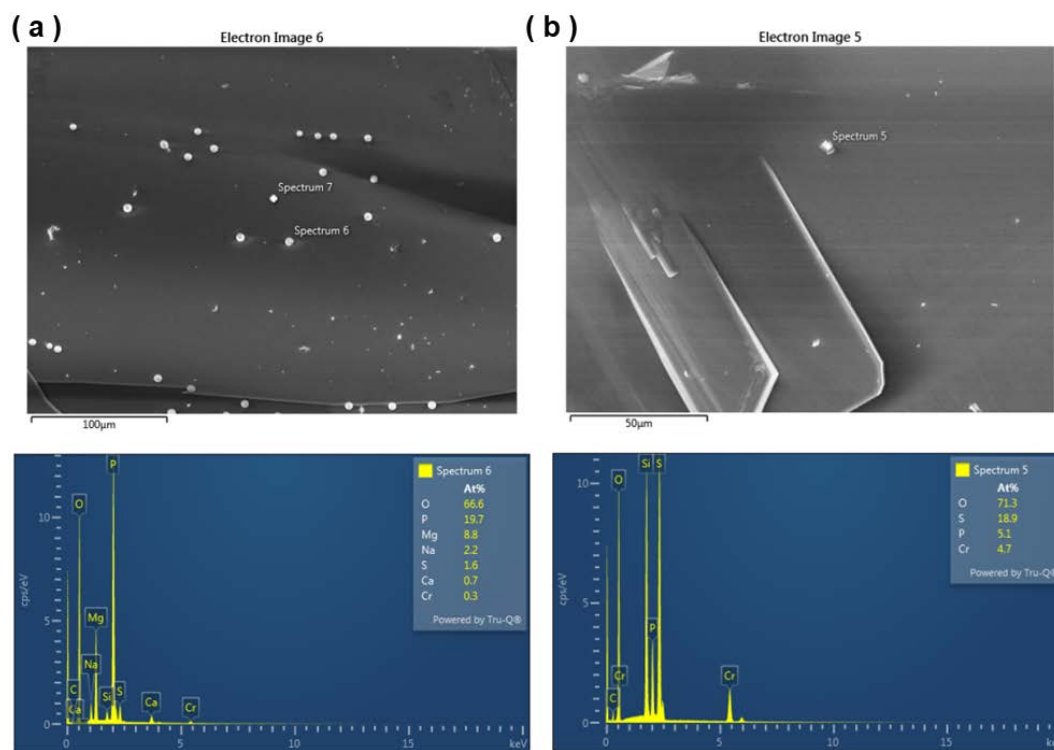


Fig. 4.9: (a) Impurities of Mg and O from sample 1 most likely present in original powder samples due to 1% impurity. (b) Glass shards from the extraction process adhered to the surface of the sample 2 crystal, characterized by Si and O atomic ratios (quartz).

atomic-scale defects in areas, and topography (surface area features). The elements and compounds of the sample, along with the relative ratios in areas, can be resolved in around one μm in diameter.

First, the ampoules were broken with a hammer, and tweezers were used to extract the crystal flakes. The flakes extracted were placed in a dish, seen in Fig. 4.4. Ampoule 1 shows slightly smaller extraction flakes when compared to ampoule 2 due to less yield and the 2D nature of the crystal structure. The samples were then analyzed through EDS. The resulting atomic ratios are seen in Fig. 4.8. Fig. 4.8 (a) shows an image of the crystal area scanned, and the resulting atomic ratios below. The scanned area was around $150 \times 150 \mu\text{m}$ for sample 1. The EDS spectrum shows peaks of Cr, P, and S, at a 1:1:4 ratio up to 6 keV. For sample 2 in Fig. 4.8, the area scanned was $250 \times 250 \mu\text{m}$, with similar atomic percentages to sample 1, giving a ratio of Cr, P, and S, at a 1:1:4 ratio. Both furnaces are presumed to have the correct bulk crystal formed of CrPS_4 .

Upon examination of the crystals, impurities were found, shown in Fig. 4.9. Fig. 4.9 (a) shows Mg and O particles on the surface of sample 1. Due to the tweezers not being thoroughly cleaned before extraction, the impurities were most likely attached to the surface transferred from the tweezers. Fig. 4.9 (b) shows sample 2 with Si and O with atomic ratios of 1:2. Quartz is the molecular compound, SiO_2 , and the impurities are presumed to be shards of quartz glass when the ampoule was broken under impact.

Chapter 5

Electronic Structure of Transition-Metal Doping in CrPS₄

In this chapter, the evolution of the electronic properties of Mn and Fe doped CrPS₄ are reported. To understand the effect of added valence electrons on the system, we dope the parent compound, CrPS₄, by replacing each Cr in the unit cell one atom at a time with Mn and Fe, separately. The doped systems are calculated using QuantumATK Atomistic simulation software[78]. To properly assess and model the doped system, we benchmark CrPS₄ in QuantumATK to ensure the software produces the correct band gap and magnetic moment for the bulk ground state of the parent compound.

5.1 Methodology and Benchmarking

Using a linear combination of atomic orbitals (LCAO) calculator, we utilize the SCAN meta-GGA functional implemented in QuantumATK with the SG15 pseudopotential set to medium. We converge the bulk CrPS₄ with a tolerance of 10^{-7} eV. The spin configuration is set to the known AFM-A ground state to calculate the magnetic moments per each Cr. The bulk CrPS₄ benchmarking results are shown in Table5.1 along with a

Table 5.1: Benchmark results for calculations executed in QuantumATK, vs. previous VASP calculations and experimental values.

Bulk CrPS ₄	Band Gap (eV)	Magnetic Moment (μ_B/Cr)
QATK - LCAO	1.36	3.21
VASP - PAW	1.32	2.78
Experimental[41]	1.40	2.81

comparison of the VASP calculations from Chapter 3 and the experimental values.

Similar to our VASP calculations, SCAN implemented into QATK predicts a band gap within 40 meV of the known band gap and a magnetic moment within reason. With these reasonable values, we proceed to dope the system with Mn and Fe replacing Cr in the unit cell one atom at a time to report the changes within the electronic structure.

5.2 Mn-doped CrPS₄

We first use Mn to dope CrPS₄. The band structure for CrPS₄ to Cr_{1-x}MnxPS₄ is shown in Fig. 5.1. The red represents the spin-up bands, and the black is the spin-down bands. The green dashed Fermi line at $y=0$ eV differentiates a metal from a non-metal material - if a band crosses over the Fermi line, the material is considered a metal. Due to the difference in atomic radii, the geometry of the Brillouin zone for the energy that is calculated within momentum space is a primitive monoclinic lattice for CrPS₄

and transforms to a primitive orthorhombic lattice, hence the path difference when the mother compound is doped; the paths within the Brillouin zone stay the same route, however from the high symmetry point route (x -axis) at X to A in CrPS₄ compared to X to U in the doped system, is slightly longer.

The first dopant of Mn from Fig. 5.1 (a) to (b) shows the gap of the system closing with extra bands from Mn existing closer to the Fermi-line and the gap becomes less than 1 eV from 1.36 eV in the mother compound. In Fig. 5.1 (b), the spin-down bands contributed from Mn lay flat in the conduction and valence bands; however, when an Mn dopant again replaces the system, the Mn bands nearer the Fermi-line become more energetic as seen in Fig. 5.1 (c) (two Mn dopants) and (d) (three Mn dopants). Due to the higher energy, the gap continues to close, in which (e) (four Mn dopants) now shows an Mn band touching the Fermi surface, where the system becomes metallic. Shown in (f) (five Mn dopants), the Mn bands continue to grow higher in energy. Now, the bands that once existed separately in the conduction and valence bands are crossing, indicating electronic bands can now pass to another band without changing their energy. This trend continues as six Mn dopants are introduced, shown in (g); interestingly, at seven Mn dopants, shown in (h), the Mn bands begin to separate near the Fermi-line and no longer crossover. Beyond this, the system produces a band gap once more for MnPS₄, which can be seen in Fig. 5.2.

We now move to the density of states shown for the evolution of the Mn-doped CrPS₄. Fig.5.2 displays (a) CrPS₄ mother compound to Cr_{1-x}Mn_x PS₄ from (b) to (h),

and (i), the DOS for MnPS₄. Here, we can see how the electron orbitals evolve and contribute to the change in the band gap into a metallic state. From Fig. 5.2 (a) CrPS₄ to (b) Cr_{0.86}Mn_{0.14}PS₄, hybridized Mn *p*- and *d*-orbitals can be seen contributing to the decreased band gap as mentioned from the band structure analysis in Fig. 5.1. Little change happens within the conduction bands. Adding a second dopant to the system, more *d*-electrons exist closer to the Fermi level, as seen from (b) to (c). This trend continues from (d) (three dopants) to (e) (four dopants), in which the increasing Mn *p*- and *d*- orbitals appear to prioritize existing at energy levels closer to the Fermi-level. The metallic system becomes obvious at (f) five Mn dopants, where the density of *d*-orbital states in the valence band has significantly decreased due to the free mobility through energetic levels in the metallic state. At (g) six dopants, the *p*-valence orbitals also begin to decrease, where now the density of *p*-orbitals in the conduction band are much more prominent, seen between 1-2 eV, showing the *p*- and *d*- orbitals in the system communicate and move through the electronic structure of the metallic state. However, when the system has seven Mn dopants, the density of states between 1-2 eV decreases, shown in (h), and the energy occupancies at the Fermi-level start to separate into the conduction and valence bands. When the structure is entirely replaced with Mn shown in (i), The electronic behavior returns to a semiconductor. MnPS₄ electronic states are now fully recognized. The *d*-orbitals in this system occupy less in the valence band and more in the conduction band than (a) CrPS₄.

5.3 Fe-doped CrPS₄

To further study the effects of added valence electrons of a transition-metal thiophosphate, we dope CrPS₄ with Fe in the same procedure as Mn. The band structure for the Fe-doped system is shown in Fig. 5.3. Unlike Mn, (b) shows Fe produces bands at the Fermi-level at just one dopant. However, at 2 Fe atoms replacing Cr (25%), a band gap of less than 0.5 eV appears, as seen in (c). The doped structure returns to a metallic state after 37.5% doping shown in (d), where energetic down (black) bands populate k -space, and crossover the Fermi-level at Γ . As the system continues to be doped with Fe, more bands populate near $E=0$, seen in (e) doping at $x = 50\%$, and bands continuously dampen as seen in the trend from (f) $x = 62.4\%$, (g) $x = 75\%$, and (h) $x = 87.5\%$. Because the bands begin to flatten, fewer electrons can move through momentum space where the system evidences the nature of a metallic state for FePS₄.

How the electrons are distributed in the system as it evolves from the semiconductor CrPS₄ to the metallic state in FePS₄ can be seen in Fig. 5.4. Fig. 5.4 (a) is the bulk CrPS₄ mother compound in comparison to the doped evolution from (b) 12.5% doping to (h) 87.5%, and finally (i), bulk FePS₄ DOS. Unlike Mn-doped CrPS₄, Cr_{1-x}Fe_xPS₄ switches to a metallic state after one Cr is replaced by Fe shown in (b). The shift in the state is contributed by the d -electrons (red) contributed by Fe, where hybridization occurs between the p - (blue) and d - electrons at the fermi-level. This hybridization is not present in (a) CrPS₄, indicating the Fe d -electrons persuade the heightened energetic occupancy into the conduction band, allowing more freedom for

the p -electrons to move through the system. However, when doped with 25% Fe shown in (c), the system returns to a semiconductor state, revealing the electrons have a weak preference toward a metallic state at this doping level and below. Above this amount of doping, (d) shows at 37.5% doping of Fe, the electrons begin to move freely to the conduction bands without additional energy as the p - and d -electrons exist at the fermi-level. This trend continues at (e) 50% doping, and in (f), the DOS reveals the population of p - and d - electrons prefer to populate at the fermi-level. However, hybridization is not present between the orbitals. In (g) at 75% doping of Fe, the density grows larger at the fermi-level and continues through at (h) 87.5% doping. The system from our model shows that FePS_4 in (i) evidences a metal material due to the p - and d orbitals.

The comparison of the changes in band gap from $x = 0.125$ to $x=1.0$ is shown in Fig. 5.5. Here, we can see the trend of the subtle decrease in Mn, shown as the green, in comparison to the Fe doped system, shown in red. system. The oscillations from both band gaps may be due to the random placement of each TM atom. causing a disruption in the electronic structure.

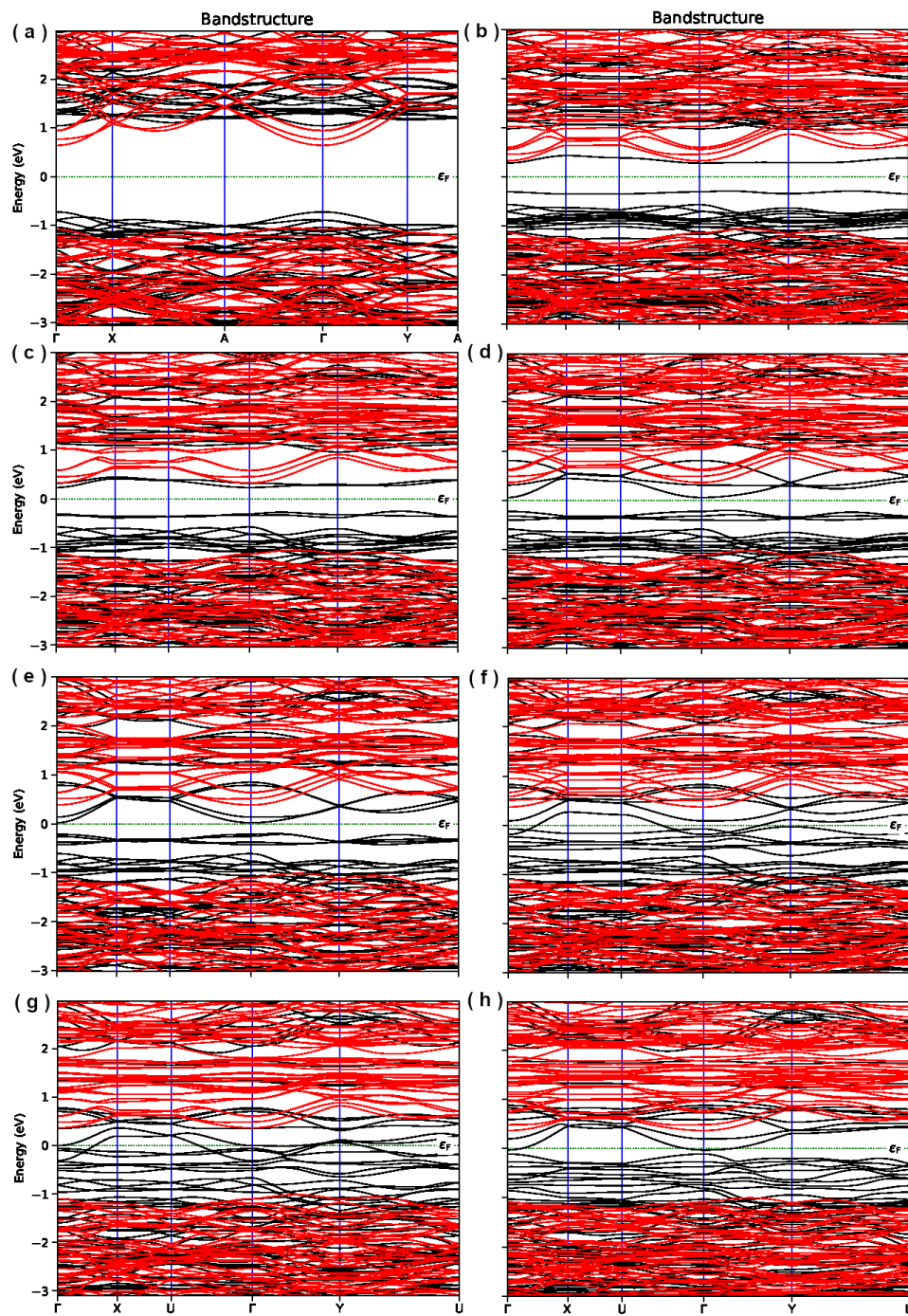


Fig. 5.1: The band structure evolution of CrPS_4 doped with Mn per each Cr site within the unit cell starting from (a) the mother compound to (h) $\text{Cr}_{(0.13)}\text{Mn}_{(0.88)}\text{PS}_4$ in steps of $x=0.125$.

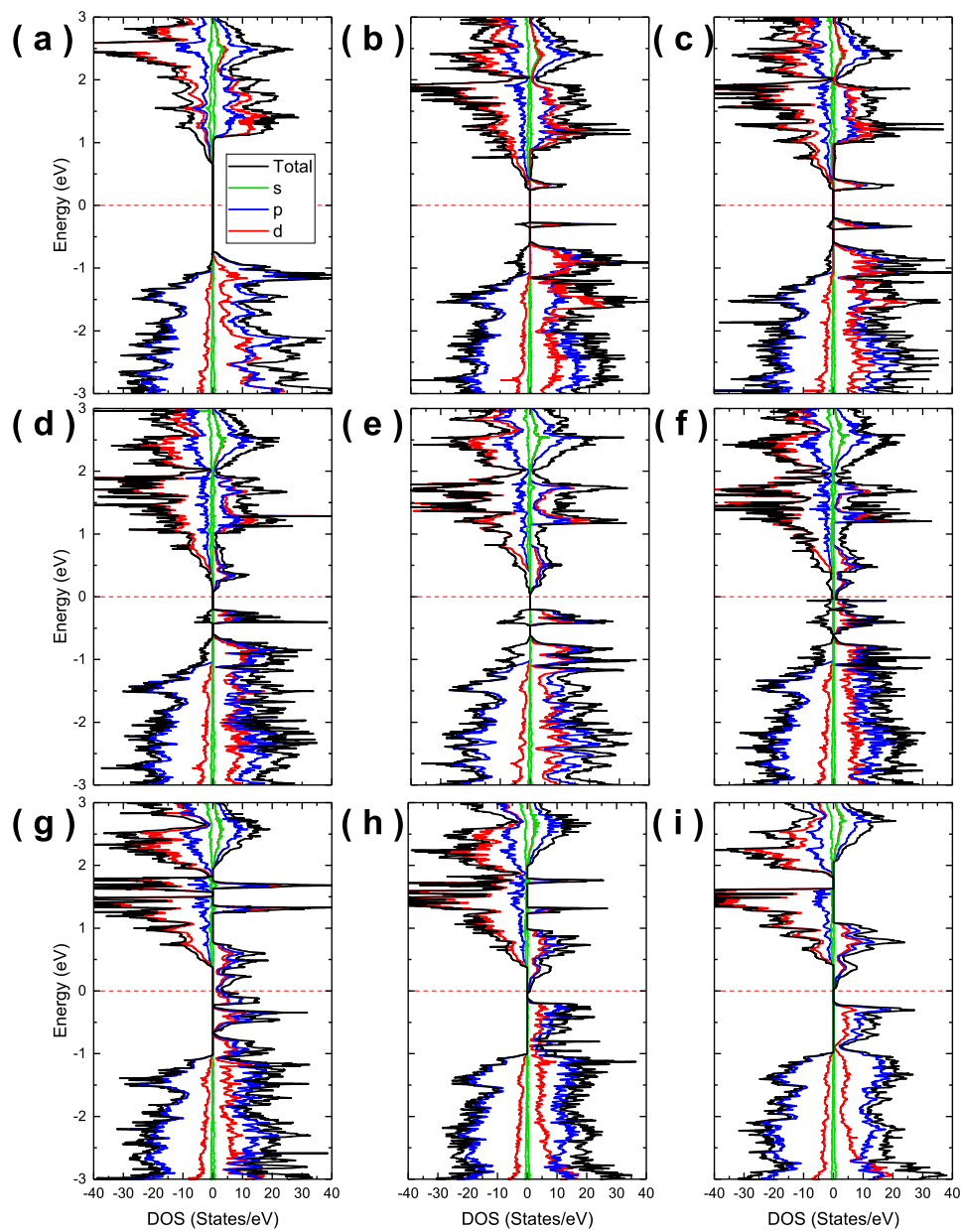


Fig. 5.2: The density of states for the doped evolution of (a) CrPS₄ (i) to MnPS₄ in steps of $x=0.125$.

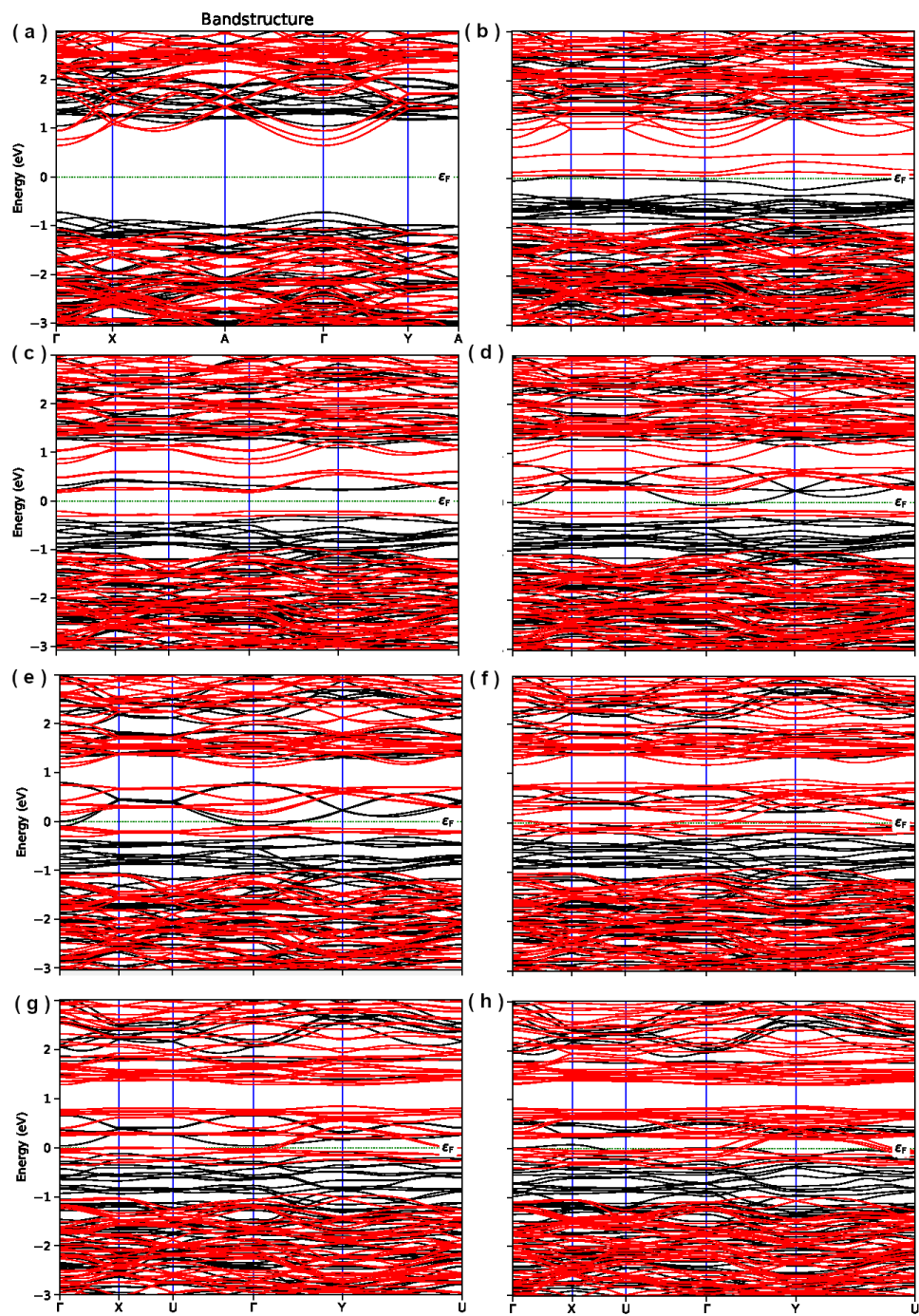


Fig. 5.3: The band structure evolution of CrPS_4 doped with Fe per each Cr site within the unit cell starting from (a) the mother compound to (h) $\text{Cr}_{(0.13)}\text{Fe}_{(0.88)}\text{PS}_4$ in steps of $x=0.125$.

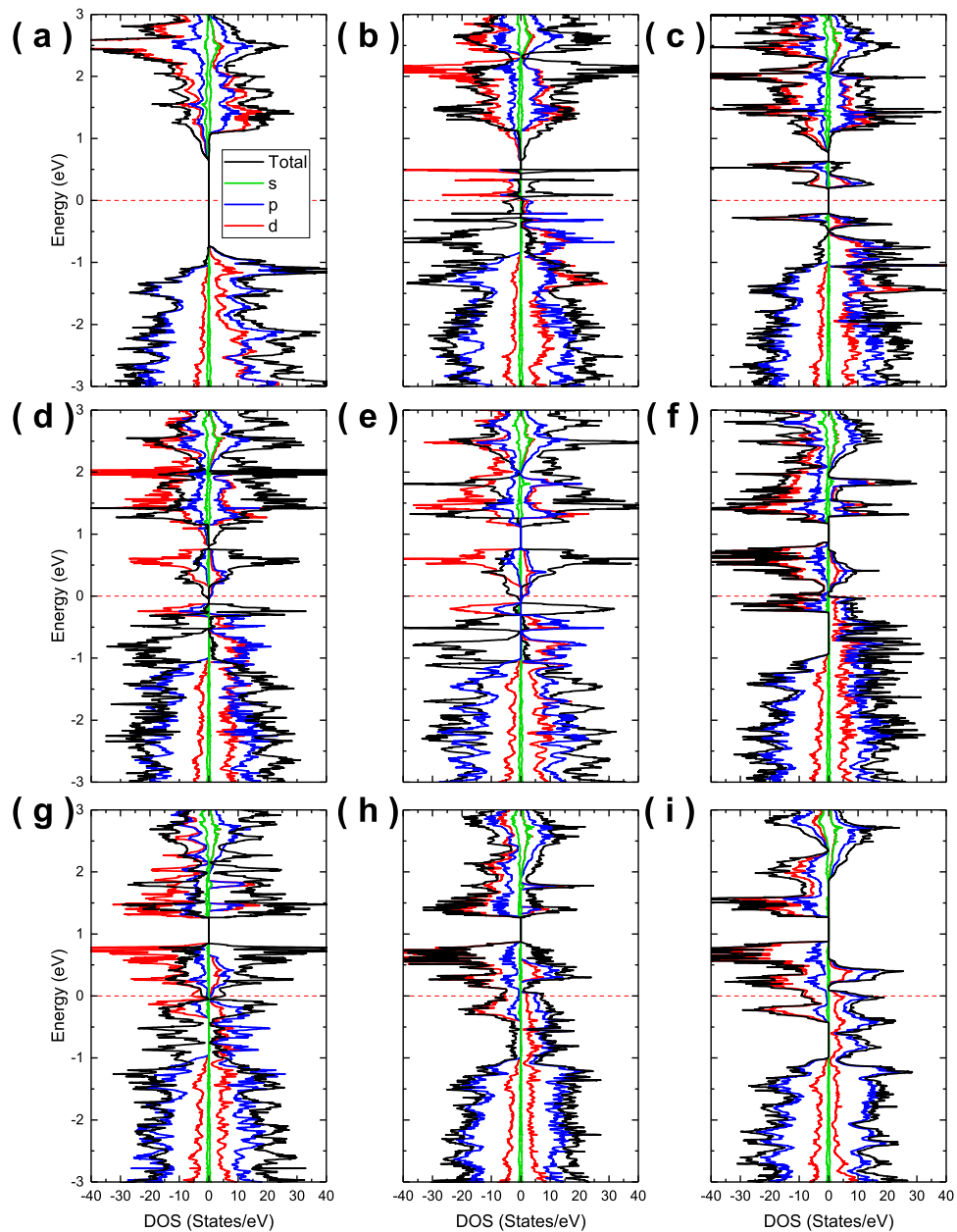


Fig. 5.4: The density of states for the doped evolution of (a) CrPS₄ to (i) FePS₄ in steps of $x=0.125$ showing how the electrons evolve toward the heavier TM compound.

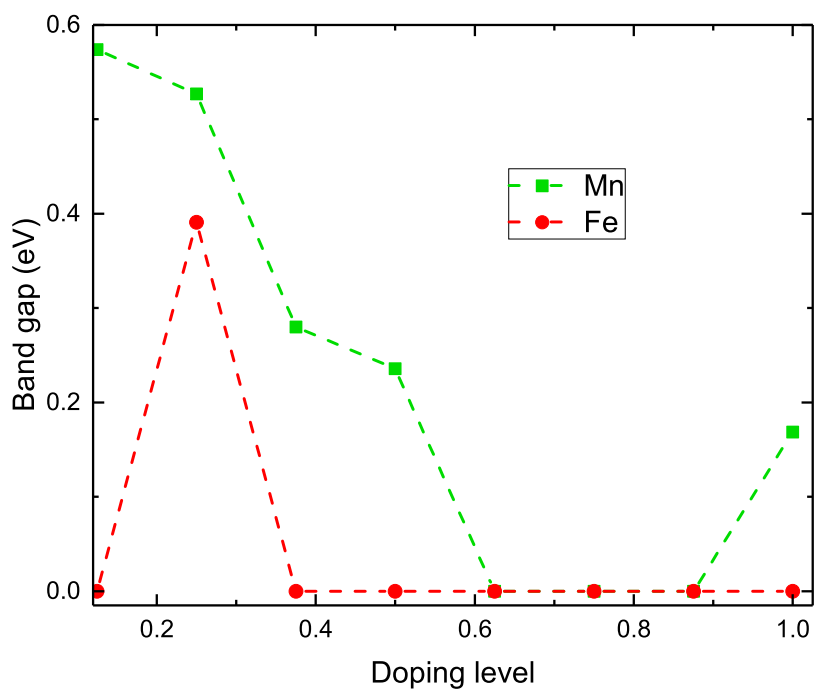


Fig. 5.5: Band gap evolution from CrPS_4 to MnPS_4 (green) and FePS_4 (red) in steps of $x=0.125$.

Chapter 6

Discussion and Conclusion

Our study has demonstrated that a first-principles parameter-free treatment of the ground state magnetic and electronic properties of the air-stable CrPS₄ 2D magnet is possible. Using the SCAN density functional, we find a major improvement over standard PBE and PBE+U approaches at nearly the same computational cost. Our study lays a firm foundation for the predictive exploration and design of new heterostructures and devices composed of CrPS₄, mitigating the need for purely experimental efforts. Furthermore, the highly anisotropic cross-coupling between spin, charge, and lattice also provides a path towards multifunctional devices ideal for monolithically integrating into semiconducting substrates for efficient interfaces between logic–interconnect – memory sectors in emerging 3D logic-memory architectures.

Furthermore, we used CVT to grow the bulk 2D magnetic crystal, CrPS₄, and demonstrate the characterization using SEM. Powder XRD was used to ensure the correct raw element powders were used in the synthesis process and compared with previous literature. Once confirmed, the powders were weighed in a 1:1:4 ratio for chromium, sulfur, and phosphorus, respectively. The glass quartz ampoules were vacuum-

sealed to 10^{-3} torr, including an argon gas source to flush out the system. Two samples were prepared and placed into two different tube furnaces of different temperature gradients to report the effect of the temperature on growth. The elements were allowed to heat over five days, during which they were turned off and then allowed to cool for two days. The SEM results revealed both ampoules contained CrPS₄ flakes, indicating marginal leeway in the success of the production of the van der Waals magnet demonstrated by furnace 1 having a temperature gradient lower than previous CrPS₄ growth studies. Furthermore, the extraction process caused impurities to attach to the surface of the crystals and should be reconsidered. Overall, we show the ease of CrPS₄ crystal growth and characterization to use in practical cases.

To go beyond current knowledge, we model the electronic structures of bulk MnPS₄ and FePS₄ by doping CrPS₄ and examining the changes within the band structure and density of states at the system evolves with the added valence electrons. The band structure and density of states for Cr_{1-x}Mn_xPS₄ reveals the evolution of the *p*- and *d*-electrons settling near the Fermi level as Mn dopants are added, to which at four total dopants, the system goes into a metallic state. However, once the system begins to become Mn-dominant (five Mn dopants to MnPS₄), the electrons begin to rearrange themselves away from the Fermi-level, settling back into a semiconductor at bulk MnPS₄. This evolution indicates that bulk MnPS₄ may exist as a semiconductor rather than a metal in a pragmatic case.

We then doped CrPS₄ with Fe using the same procedure of replacing one Cr

atom with Fe to examine the system's band structure and density of states with two extra valence electrons compared to Cr. Shown from the band structure, the electronic system moves toward a metallic system at less than 50% Fe doping, unlike Mn. Doping at and above 50% Fe for the thiophosphate compound indicates a metal for the Fe^{3+} oxidation state in this compound from the BS and DOS, revealing FePS_4 may not exist as a semiconductor.

Overall, we study CrPS_4 in its bulk and few-layer form through theory and synthesis characterization. Our DFT study reveals the efficiency of the SCAN meta-GGA functional on the well-studied magnetic material using experimental values as benchmarking, demonstrating an enhanced predictive method for theoretical models for 2D magnetic materials. Our experimental procedure exhibits the practicality of growth and stability of bulk CrPS_4 . Due to the success of bulk and few-layer CrPS_4 in theory and experiment, we end this study with the motivation to examine the electronic structure of two transition-metal thiophosphate bulk compounds, MnPS_4 and FePS_4 , in which our DFT methods reveal MnPS_4 to have a narrow band gap of less than 1 eV, and FePS_4 to be a metal material.

Bibliography

- [1] H. Zhuang and J. Zhou. Density functional theory study of bulk and single-layer magnetic semiconductor CrPS₄. *Physical Review B*, 94:195307, 2016.
- [2] M. Joe, H. Lee, M. Alyoruk, J. Lee, S. Kim, C. Lee, and J. Lee. A comprehensive study of piezomagnetic response in CrPS₄ monolayer: mechanical, electronic properties and magnetic ordering under strains. *JoP: Condensed Matter*, 29:405801, 2017.
- [3] Evgeny Elsukov, Denis Kolodkin, Alexander Ul'yanov, and Vitaly Porsev. Probe Mössbauer spectroscopy of mechanical alloying in binary Cr₋₅₇Fe (1 at%) system. *AIP Conference Proceedings*, 1622:114–119, 10 2014.
- [4] Ta Bao, Ojin Tegus, Hasichaolu, Jun Ning, and Narengerile. Preparation of Black Phosphorus by the Mechanical Ball Milling Method and its Characterization. *Solid State Phenomena*, 271:18–22, 01 2018.
- [5] Akl Awwad. Noval Approach For Synthesis Sulfur (S-NPs) Nanoparticles Using Albizia Julibrissin Fruits Extract. *Adv Mater Lett*, 6:235–238, 05 2015.
- [6] Marius Grundmann. *The Physics of Semiconductors*. Springer, 2010.
- [7] J. T. Wollmark. Is there a minimum linewidth in integrated circuits? *New Developments in Semiconductor Physics. Lecture Notes in Physics*, 122:263–276, 2005.
- [8] J. R. Tucker, C. Wang, and P. S. Carney. Silicon field-effect transistor based on quantum tunneling. *Appl. Phys. Lett.*, 65(5):618–620, 1994.
- [9] T. Saga. Advances in crystalline silicon solar cell technology for industrial mass production. *NPG Asia Materials*, 2:96–102, 2010.
- [10] Y. Chen, P. Altermatt, D. Chen, X. Zhang, Z. Feng, H. Shen, and P. Verlinden. From Laboratory to Production: Learning Models of Efficiency and Manufacturing Cost of Industrial Crystalline Silicon and Thin-Film Photovoltaic Technologies. *IEEE Journal of Photovoltaics*, 8(6):1531–1538, 2018.

- [11] K. Whitener Jr. and P. Sheehan. Graphene synthesis. *Diamond and Related Materials*, 46:25–34, 2014.
- [12] Y. Hwang and J. Kim. Enhancement of thermal and mechanical properties of flexible graphene oxide/carbon nanotube hybrid films through direct covalent bonding. *J. Mater. Sci.*, 48:7011–7021, 2013.
- [13] X. Yang, A. Vorobiev, A. Generalov, M. Andersson, and J. Stake. A flexible graphene terahertz detector. *Appl. Phys. Lett.*, 111:021102, 2017.
- [14] N. Petrone, I. Meric, T. Chari, K. Shepard, and J. Hone. Graphene and Field-Effect Transistors for Radio-Frequency Flexible Electronics. *IEEE Journal of the Electron Devices Society*, 3(1):44–48, 2015.
- [15] R. Mas-Balleste, C. Gomez-Navarro, J. Gomez-Herrero, and F. Zamora. 2D materials: to graphene and beyond. *Nanoscale*, 3:20–30, Sep. 2010.
- [16] P. Avouris, T. Heinz, and T. Low. *2D Materials*. Cambridge University Press, 2017.
- [17] M. Gibertini, M. Koperski, A. Morpurgo, and K. Novoselov. Magnetic 2D materials and heterostructures. *Nat. Nanotechnol.*, 14:408–419, May 2019.
- [18] D. Akinwande and *et.al*. A review on mechanics and mechanical properties of 2D materials—Graphene and beyond. *Elsevier*, 13:42–77, May 2017.
- [19] C. Dean, A. Young, I. Meric, C. Lee, L. Wang, S. Sorgenfrei, K. Watanabe, T. Taniguchi, P. Kim, K. Shepard, and J. Hone. Boron nitride substrates for high-quality graphene electronics. *Nature Nanotechnology*, 5:722–726, 2010.
- [20] A. Splendiani and *et. al*. Emerging Photoluminescence in Monolayer MoS₂. *Nano Lett.*, 10:1271–1275, 2010.
- [21] Y. Illarionov, T. Knobloch, M. Jech, M. Lanza, D. Akinwande, M. Vexler, T. Mueller, M. Lemme, F. Fiori, G. and Schwierz, and T. Grasser. Insulators for 2D nanoelectronics: the gap to bridge. *Nature Communications*, 11:3385, 2020.
- [22] S. Kang, D. Lee, H. Kim, A. Capasso, H. Kang, J. Park, C. Lee, and G. Lee. 2D semiconducting materials for electronic and optoelectronic applications: potential and challenge. *2D Materials*, 7:022003, 2020.
- [23] X. Liu and M. Hersam. 2D materials for quantum information science. *Nature Reviews Materials*, 4:669–684, 2019.

- [24] K. Buapan, R. Somphonsane, T. Chiawchan, and H. Ramamoorthy. Versatile, Low-Cost, and Portable 2D Material Transfer Setup with a Facile and Highly Efficient DIY Inert-Atmosphere Glove Compartment Option. *ACS Omega*, 6: 17952–17964, 2021.
- [25] D. Geng and H. Yang. Recent Advances in Growth of Novel 2D Materials: Beyond Graphene and Transition Metal Dichalcogenides. *Adv. Mater.*, 30:1800865, Nov. 2018.
- [26] W. Choi, N. Choudhary, G. Han, J. Park, D. Akinwande, and Y. Lee. Recent development of two-dimensional transition metal dichalcogenides and their applications. *materialstoday*, 20:116–130, Apr. 2017.
- [27] G. Cassabois, P. Valvin, and B. Gil. Hexagonal boron nitride is an indirect bandgap semiconductor. *Nature photonics*, 10(4):262–266, 2016.
- [28] M. Khan, S. Ali, N. Alwadai, M. Irfan, H. Albalawi, A. Almuqrin, M. Almoneef, and M. Iqbal. Structural, electrical and optical properties of hetrostructured MoS₂/ZnO thin films for potential perovskite solar cells application. *Journal of Materials Research and Technology*, 20:1616–1623, 2022.
- [29] M. Zhao, W. Xia, Y. Wang, M. Luo, Z. Tian, Y. Guo, W. Hu, and J. Xue. Nb₂SiTe₄: a stable narrow-gap two-dimensional material with ambipolar transport and mid-infrared response. *ACS nano*, 13(9):10705–10710, 2019.
- [30] Q. Wang, K. Kalantar-Zadah, A. Kis, J. Coleman, and M. Strano. Electronics and optoelectronics of two-dimensional transition metal dichalcogenides. *Nature Nanotechnology*, 7:699–712, 2012.
- [31] X. Duan, C. Wang, J. Shaw, R. Cheng, Y. Chen, H. Li, X. Wu, Y. Tang, Q. Zhang, A. Pan, J. Jiang, R. Yu, Y. Huang, and X. Duan. Lateral epitaxial growth of two-dimensional layered semiconductor heterojunctions. *Nature nanotechnology*, 9: 1024–1030, 2014.
- [32] S. Manzeli, D. Ovchinnikov, P. Diego, O. Yazyev, and A. Kis. 2D transition metal dichalcogenides. *Nature Reviews Materials*, 2:17033, Jun. 2017.
- [33] B. Ozdemir and V. Barone. Thickness dependence of solar cell efficiency in transition metal dichalcogenides MX₂ (M: Mo, W; X: S, Se, Te). *Elsevier*, 212:110557, 2020.
- [34] K. Mak and J. Shan. Photonics and optoelectronics of 2D semiconductor transition metal dichalcogenides. *Nature Photonics*, 10:216–226, Mar. 2016.

- [35] Yangmu Li, Nader Zaki, Vasile O Garlea, Andrei T Savici, David Fobes, Zhijun Xu, Fernando Camino, Cedomir Petrovic, Genda Gu, Peter D Johnson, et al. Electronic properties of the bulk and surface states of $\text{Fe}_{1+y}\text{Te}_{1-x}\text{Se}_x$. *Nature Materials*, 20(9):1221–1227, 2021.
- [36] Kyoo Kim, Junho Seo, Eunwoo Lee, K-T Ko, BS Kim, Bo Gyu Jang, Jong Mok Ok, Jinwon Lee, Youn Jung Jo, Woun Kang, et al. Large anomalous hall current induced by topological nodal lines in a ferromagnetic van der waals semimetal. *Nature materials*, 17(9):794–799, 2018.
- [37] Kenneth S Burch, David Mandrus, and Je-Geun Park. Magnetism in two-dimensional van der waals materials. *Nature*, 563(7729):47–52, 2018.
- [38] Dmitry Shcherbakov, Petr Stepanov, Daniel Weber, Yaxian Wang, Jin Hu, Yanglin Zhu, Kenji Watanabe, Takashi Taniguchi, Zhiqiang Mao, Wolfgang Windl, et al. Raman spectroscopy, photocatalytic degradation, and stabilization of atomically thin chromium tri-iodide. *Nano letters*, 18(7):4214–4219, 2018.
- [39] N. Mahammad, A. Mahamad, A. Kadhum, and K. Loh. A review on synthesis and characterization of solid acid materials for fuel cell applications. *Journal of Power Sources*, 322:77–92, 2016.
- [40] K. Du, X. Qang, Y. Liu, P. Hu, I. Utama, C. Gan, Q. Xiong, and C. Kloc. Weak Van der Waals Stacking, Wide-Range Band Gap, and Raman Study on Ultrathin Layers of Metal Phosphorus Trichalcogenides. *ACS Nano*, 10:1738–1743, 2016.
- [41] S. Calder, A. Haglund, Y. Liu, D. Pajerowski, H. Cau, T. Williams, V. Garlea, and D. Mandrus. Magnetic structure and exchange interactions in the layered semiconductor CrPS_4 . *Physical Review B*, 102:024408, 2020.
- [42] J. Son, S. Son, P. Park, M. Kim, Z. Tao, J. Oh, T. Lee, S. Lee, J. Kim, K. Zhang, K. Cho, T. Kamiyama, J. Lee, K. Mak, J. Shan, M. Kim, J. Park, and J. Lee. Air-Stable and Layer-Dependent Ferromagnetism in Atomically Thin van der Waals CrPS_4 . *ACS Nano*, 15:16904–16912, 2021.
- [43] A. Budniak, N. Killileaw, S. Zelewski, M. Syntnyk, Y. Kauffmann, Y. Amouyal, R. Kudrawiec, W. Heiss, and E. Lifshitz. Exfoliated CrPS_4 with Promising Photoconductivity. *Nano Micro Small*, 16:1905924, 2020.
- [44] Q. Pei, X. Luo, G. Lin, J. Song, L. Hu, Y. Zou, L. Yu, W. Yong, W. Song, W. Lu, and Y. Sun. Spin dynamics, electronic, and thermal transport properties of two-dimensional CrPS_4 single crystal. *Journal of Applied Physics*, 119:043902, 2016.
- [45] J. Lee, T. Ko, J. Kim, H. Bark, B. Kang, S. Jung, T. Park, Z. Lee, S. Ryu, and C. Lee. Structural and Optical Properties of Single- and Few-layer Magnetic Semiconductor CrPS_4 . *ACS Nano*, 11:10935–10944, 2017.

- [46] Pingfan Gu, Qinghai Tan, Yi Wan, Ziling Li, Yuxuan Peng, Jiawei Lai, Junchao Ma, Xiaohan Yao, Shiqi Yang, Kai Yuan, et al. Photoluminescent quantum interference in a van der waals magnet preserved by symmetry breaking. *ACS nano*, 14(1):1003–1010, 2019.
- [47] S. Kim, J. Lee, G. Jin, M. Jo, C. Lee, and S. Ryu. Crossover between Photochemical and Photothermal Oxidations of Atomically Thin Magnetic Semiconductor CrPS₄. *Nano Letters*, 19:4043–4051, 2019.
- [48] Sujin Kim, Jinhwan Lee, Changgu Lee, and Sunmin Ryu. Polarized Raman spectra and complex Raman tensors of antiferromagnetic semiconductor CrPS₄. *The Journal of Physical Chemistry C*, 125(4):2691–2698, 2021.
- [49] Hanlin Zhang, Yong Li, Xiaozong Hu, Junmin Xu, Lijie Chen, Gang Li, Shiqi Yin, Jiawang Chen, Chaoyang Tan, Xucai Kan, et al. In-plane anisotropic 2D CrPS₄ for promising polarization-sensitive photodetection. *Applied Physics Letters*, 119(17):171102, 2021.
- [50] Minjeong Shin, Mi Jung Lee, Chansoo Yoon, Sohwi Kim, Bae Ho Park, Sungmin Lee, and Je-Geun Park. Charge-trapping memory device based on a heterostructure of MoS₂ and CrPS₄. *Journal of the Korean Physical Society*, 78(9):816–821, 2021.
- [51] Maurizio Riesner, Rachel Fainblat, Adam K Budniak, Yaron Amouyal, Efrat Lifshitz, and Gerd Bacher. Temperature dependence of Fano resonances in CrPS₄. *The Journal of Chemical Physics*, 156(5):054707, 2022.
- [52] Suhyeon Kim, Sangho Yoon, Hyobin Ahn, Gangtae Jin, Hyesun Kim, Moon-Ho Jo, Changgu Lee, Jonghwan Kim, and Sunmin Ryu. Photoluminescence Path Bifurcations by Spin Flip in Two-Dimensional CrPS₄. *ACS nano*, 2022.
- [53] Guoliang Xu, Danmin Liu, Songyu Li, Yi Wu, Zhenlu Zhang, Shaobo Wang, Zikun Huang, and Yongzhe Zhang. Binary-ternary transition metal chalcogenides interlayer coupling in van der waals type-ii heterostructure for visible-infrared photodetector with efficient suppression dark currents. *Nano Research*, 15(3):2689–2696, 2022.
- [54] Q. Chen, Q. Ding, Y. Wang, Y. Xu, and J. Wang. Electronic and Magnetic Properties of a Two-Dimensional Transition Metal Phosphorous Chalcogenide TMPS₄. *J. Phys. Chem. C*, 124:12075–12080, May 2020.
- [55] Jun Deng, Jiangang Guo, Hideo Hosono, Tianping Ying, and Xiaolong Chen. Two-dimensional bipolar ferromagnetic semiconductors from layered antiferromagnets. *Physical Review Materials*, 5(3):034005, 2021.

- [56] Jie Yang, Shibo Fang, Yuxuan Peng, Shiqi Liu, Baochun Wu, Ruge Quhe, Shilei Ding, Chen Yang, Jiachen Ma, Bowen Shi, and *et. al.* Layer-Dependent Giant Magnetoresistance in Two-Dimensional CrPS₄ Magnetic Tunnel Junctions. *Physical Review Applied*, 16(2):024011, 2021.
- [57] A. Louisy, G. Ouvrard, D. Schleich, and R. Brec. Physical properties and lithium intercalates of CrPS₄. *Solid State Communications*, 28:61–66, 1978.
- [58] M. Lee, S. Lee, S. Lee, K. Balamurugan, C. Yoon, J. Jang, S. Kim, D. Kwon, M. Kim, J. Ahn, D. Kim, J. Park, and B. Park. Synaptic devices based on two-dimensional layered single-crystal chromium thiophosphate (CrPS₄). *NPG Asia Materials*, 10:23–30, 2018.
- [59] D. R. Hartree. The Wave Mechanics of an Atom with a Non-Coulomb Central Field. Part II. Some Results and Discussion. *Mathematical Proceedings of the Cambridge Philosophical Society*, 24(1):111–132, 1928.
- [60] W. Kohn and L. J. Sham. Self-consistent equations including exchange and correlation effects. *Phys. Rev.*, 140:A1133–A1138, Nov 1965.
- [61] P. Hohenberg and W. Kohn. Inhomogeneous Electron Gas. *Phys. Rev.*, 136:B864–B871, Nov 1964.
- [62] R. Diehl and C. Carpentier. The Crystal Structure of Chromium Thiophosphate, CrPS₄. *Acta Crystallographica Section B*, B33:1399–1404, 1976.
- [63] G. Kresse and D. Joubert. From ultrasoft pseudopotentials to the projector augmented-wave method. *Physical Review B*, 59:1758, 1999.
- [64] G. Kresse and J. Hafner. *Ab initio* molecular dynamics for open-shell transition metals. *Physical Review B*, 48:13115, 1993.
- [65] G. Kresse and J. Furthmuller. Efficient iterative schemes for *ab initio* total-energy calculations using a plane-wave basis set. *Physical Review B*, 54:11169, 1996.
- [66] J. Sun, A. Ruzsinszky, and J. Perdew. Strongly Constrained and Appropriately Normed Semilocal Density Functional. *Physical Review Letters*, 115:036402, 2015.
- [67] A.R. Alcantara, C. Lane, J.T. Haraldsen, and R.M. Tutchton. Parameter free treatment of a layered correlated van der Waals magnet: CrPS₄. *TBD*, 2023.
- [68] Andreas Görling. Exact treatment of exchange in kohn-sham band-structure schemes. *Physical Review B*, 53(11):7024, 1996.

- [69] John P Perdew, Weitao Yang, Kieron Burke, Zenghui Yang, Eberhard KU Gross, Matthias Scheffler, Gustavo E Scuseria, Thomas M Henderson, Igor Ying Zhang, Adrienn Ruzsinszky, and *et. al.* Understanding band gaps of solids in generalized kohn–sham theory. *Proceedings of the national academy of sciences*, 114(11): 2801–2806, 2017.
- [70] J Zaanen, GA Sawatzky, and JW Allen. Band gaps and electronic structure of transition-metal compounds. *Physical review letters*, 55(4):418, 1985.
- [71] James L Erskine and EA Stern. Calculation of the m23 magneto-optical absorption spectrum of ferromagnetic nickel. *Physical Review B*, 12(11):5016, 1975.
- [72] Jing Xia, Yoshiteru Maeno, Peter T Beyersdorf, MM Fejer, and Aharon Kapitulnik. High resolution polar Kerr effect measurements of Sr_2RuO_4 : Evidence for broken time-reversal symmetry in the superconducting state. *Physical review letters*, 97(16):167002, 2006.
- [73] Davide Sangalli, Andrea Marini, and Alberto Debernardi. Pseudopotential-based first-principles approach to the magneto-optical kerr effect: From metals to the inclusion of local fields and excitonic effects. *Physical Review B*, 86(12):125139, 2012.
- [74] Christopher Lane and Jian-Xin Zhu. Thickness dependence of electronic structure and optical properties of a correlated van der Waals antiferromagnetic NiPS_3 thin film. *Physical Review B*, 102(7):075124, 2020.
- [75] O. A. Sergeev, A. Shashkov, and A. Umanskii. Thermophysical properties of quartz glass. *Journal of engineering physics*, 43:1375–1383, 1982.
- [76] W. Schnelle, J. Engelhardt, and E. Gmelin. Specific heat capacity of Apiezon N high vacuum grease and of Duran borosilicate glass. *Cryogenics*, 39:271–275, 1999.
- [77] A. Arrot, S. Werner, and H. Kendrick. First-order magnetic phase change in chromium at 38.5 C. *Physical Review Letters*, 14:1022, 1965.
- [78] S. Smidstrup, T. Markussen, P. Vancraeyveld, J. Wellendorff, J. Schneider, T. Gunst, B. Verstichel, D. Stradi, P. Khomyakov, and U. Vej-Hansen. QuantumATK: An integrated platform of electronic and atomic-scale modelling tools. *J. Phys: Condens. Matter*, 32:015901, 2020.